AGU PUBLICATIONS

Paleoceanography

RESEARCH ARTICLE
10.1002/2014PA002743

Key Points:
- Inverse methods quantify information about past circulations from tracer proxies
- Benthic tracer records constrain surface properties where deep water is formed
- A set of oxygen isotope records does not diagnose deglacial circulation changes

Correspondence to:
D. E. Amrhein,
amrhein@mit.edu

Citation:
Amrhein, D. E., G. Gebbie, O. Marchal, and C. Wunsch (2015), Inferring surface water equilibrium calcite δ^{18}O during the last deglacial period from benthic foraminiferal records: Implications for ocean circulation, *Paleoceanography*, *30*, doi:10.1002/2014PA002743.

Received 23 OCT 2014
Accepted 14 SEP 2015
Accepted article online 19 SEP 2015

Inferring surface water equilibrium calcite δ^{18}O during the last deglacial period from benthic foraminiferal records: Implications for ocean circulation

Daniel E. Amrhein[1], Geoffrey Gebbie[2], Olivier Marchal[2], and Carl Wunsch[3]

[1]Massachusetts Institute of Technology-Woods Hole Oceanographic Institution Joint Program in Oceanography, Cambridge, Massachusetts, USA, [2]Woods Hole Oceanographic Institution, Woods Hole, Massachusetts, USA, [3]Department of Earth and Planetary Sciences, Harvard University, Cambridge, Massachusetts, USA

Abstract The ocean circulation modifies mixed layer (ML) tracer signals as they are communicated to the deep ocean by advection and mixing. We develop and apply a procedure for using tracer signals observed "upstream" (by planktonic foraminifera) and "downstream" (by benthic foraminifera) to constrain how tracer signals are modified by the intervening circulation and, by extension, to constrain properties of that circulation. A history of ML equilibrium calcite δ^{18}O ($\delta^{18}O_c$) spanning the last deglaciation is inferred from a least-squares fit of eight benthic foraminiferal $\delta^{18}O_c$ records to Green's function estimated for the modern ocean circulation. Disagreements between this history and the ML history implied by planktonic records would indicate deviations from the modern circulation. No deviations are diagnosed because the two estimates of ML $\delta^{18}O_c$ agree within their uncertainties, but we suggest data collection and modeling procedures useful for inferring circulation changes in future studies. Uncertainties of benthic-derived ML $\delta^{18}O_c$ are lowest in the high-latitude regions chiefly responsible for ventilating the deep ocean; additional high-resolution planktonic records constraining these regions are of particular utility. Benthic records from the Southern Ocean, where data are sparse, appear to have the most power to reduce uncertainties in benthic-derived ML $\delta^{18}O_c$. Understanding the spatiotemporal covariance of deglacial ML $\delta^{18}O_c$ will also improve abilities of $\delta^{18}O_c$ records to constrain deglacial circulation.

1. Introduction

Changes in the physical and chemical properties of the ocean were an important component of the global climate change of the last deglaciation, the period roughly 20–10 cal kyr B.P. (ka), when Earth's atmosphere and ocean warmed and ice sheets retreated. Numerous studies have investigated possible large deviations from the modern circulation during this time using numerical models [*Manabe and Stouffer*, 1988; *Otto-Bliesner et al.*, 2007; *Liu et al.*, 2009; *Barker et al.*, 2009], proxy observations [*Keigwin*, 2004; *McManus et al.*, 2004; *Curry and Oppo*, 2005], and combinations of models and data [*LeGrand and Wunsch*, 1995; *Winguth et al.*, 2000; *Gebbie and Huybers*, 2006; *Burke et al.*, 2011; *Marchal and Curry*, 2008; *Dail and Wunsch*, 2014; *Gebbie*, 2014]. Distinguishing between possible circulation changes is challenging because the available database is sparse and has numerous sources of uncertainty.

The oxygen isotope ratio, δ^{18}O, of foraminiferal shells extracted from sediment cores has been used for decades as an indicator of global ice volume and deglacial climate change [e.g., *Hays et al.*, 1976]. Foraminiferal measurements of δ^{18}O are a proxy for the equilibrium calcite oxygen isotope ratio, $\delta^{18}O_c$, which is a function of the temperature and the oxygen isotope ratio, $\delta^{18}O_w$, of ambient seawater [e.g., *Bemis et al.*, 1998]. Increasing temperatures and melting land ice sheets both decrease $\delta^{18}O_c$ in the surface ocean, so that changes in $\delta^{18}O_c$ are indicative of major deglacial climate change processes.

Regional variations in observations of benthic $\delta^{18}O_c$ have been interpreted in terms of various physical processes and changes, including (1) changes in ocean circulation, (2) changes in mixed layer (ML) $\delta^{18}O_c$ values, (3) delays due to ocean tracer propagation times, and (4) observational, representational, and age model errors. *Skinner and Shackleton* [2005] suggested that an apparent 4000-year offset in the onset of deglaciation between $\delta^{18}O_c$ in sediment cores TR163-31B (3210 m, eastern equatorial Pacific) and MD99-2334K (3146 m, Iberian Margin) could be explained by circulation changes in the deep Atlantic Ocean.

Waelbroeck et al. [2006] interpreted reductions at 16 ka in $\delta^{18}O_c$ and the carbon isotope ratio $\delta^{13}C$ at site MD98-2165 (2100 m, Indian Ocean) as the signature of a poorly ventilated, brine-generated intermediate water mass that propagated to the Indian Ocean from the North Atlantic via a "fast connection" (simultaneous to within dating uncertainty). *Waelbroeck et al.* [2011] found signals of the last deglaciation in the Atlantic appearing earliest in waters at roughly 1000 m water depth and concluded that a delayed onset of deglaciation in waters deeper than 3000 m is consistent with reduced advection of $\delta^{18}O_c$ signals in deep waters during Heinrich Stadial 1 (17.5–16.5 ka). In contrast, *Wunsch and Heimbach* [2008] estimated time scales of tracer equilibration and concluded that the 4000-year offset in cores MD99-2334K and TR163-31B is consistent with the modern ocean circulation, and *Gebbie* [2012] found deglacial histories of global ML seawater $\delta^{18}O$ and temperature that reproduced the offset.

This paper evaluates the ability of last deglacial $\delta^{18}O_c$ records to constrain hydrographic changes hypothesized in the literature. Planktonic and benthic records lie "upstream" and "downstream" in the global ocean tracer transport in the sense that tracer values are first set in the mixed layer, near the habitats of planktonic foraminifera, and are subsequently transported to abyssal habitats of benthic foraminifera. Modifications in ML $\delta^{18}O_c$ signals as they are communicated to the deep ocean are set by properties of the ocean circulation; in principle, some of these properties can be estimated by comparing upstream and downstream observations of $\delta^{18}O_c$. An analog is a one-dimensional advective-diffusive system ("pipe flow") with transiting tracer pulses, wherein the degree of smoothing of an upstream tracer signal en route to a downstream observer is related to flow diffusivity and delays in arrival times are indicative of flow speed. Relationships between arrival times, smoothing, and transport properties are much more complex in the turbulent, three-dimensional global ocean. Here, rather than attempting directly to infer flow speeds or diffusivities, we develop an upstream-downstream framework to address the more basic question of whether a compilation of deglacial benthic and planktonic records can detect differences between the modern circulation and that of the last deglaciation. Equivalently, the goal is to test the null hypothesis that the circulation over the last deglaciation is indistinguishable from the modern circulation given the available data.

The procedure is to compare deglacial ML $\delta^{18}O_c$ histories from (1) a least-squares fit of eight benthic $\delta^{18}O_c$ benthic records to an estimate of the modern circulation and (2) 13 planktonic $\delta^{18}O_c$ records. Disagreements (beyond uncertainty) between benthic- and planktonic-derived ML $\delta^{18}O_c$ estimates would disprove the null hypothesis and provide information about deglacial circulation changes.

In the present application, ML $\delta^{18}O_c$ estimates derived from planktonic and benthic foraminifera agree given their uncertainties. This result does not mean that the circulation did not change over the deglaciation, merely that the data and assumptions lack the power to detect those changes. As additional data are gradually being generated and new age models constructed, this study should be regarded as providing a tentative set of conclusions about the power of foraminiferal $\delta^{18}O_c$ to constrain past circulations and establishing a very general method for using additional data as they become available. The main contributions of this work are a means to quantify uncertainty in the problem of inferring past circulation from ocean tracer records, an understanding of physical processes contributing to that uncertainty, and the identification of steps to reduce uncertainty in future studies.

2. Benthic and Planktonic $\delta^{18}O_c$ Records

Eight sediment core records of benthic $\delta^{18}O_c$ (Table 1) were selected based on their resolution in time (to minimize errors due to aliasing) and the availability of age models that were not derived by synchronizing $\delta^{18}O_c$ records to benthic $\delta^{18}O_c$ at other core sites, which can destroy information about the timing of tracer signals. These data are a representative, but not complete, subset of previously studied records satisfying these criteria. Most have been used in previous studies on the propagation of $\delta^{18}O_c$ signals in the ocean [*Skinner and Shackleton*, 2005; *Waelbroeck et al.*, 2006, 2011]. The data coverage is far from ideally suited to the problem; discussion of an ideal set of core locations is postponed until section 5. All $\delta^{18}O_c$ values are reported and plotted in units of permil Vienna Peedee belemnite (VPDB).

For easier reference, benthic records are labeled in this study by ocean basin and recovery depth rather than cruise number (e.g., SA3770 is the core recovered from the South Atlantic at 3770 m water depth; see Table 1). Five of the records were obtained from the Atlantic Ocean, two from the Indian Ocean, and one from the Pacific Ocean (Figure 1). Water depths of the sediment cores range from 1299 m to 3770 m. All of the records

Table 1. Summary of Benthic Foraminiferal $\delta^{18}O_c$ Records[a]

Core	Code	Ocean	Depth	Species	References
GeoB1711	SA1967	Atl S	1967 m	*Cibicidoides wuellerstorfi*	*Little et al.* [1997]
					Vidal et al. [1999]
					Waelbroeck et al. [2006]
GeoB9526-4	NA3223	Atl N	3223 m	*C. wuellerstorfi*	*Zarriess and Mackensen* [2010]
					Zarriess and Mackensen [2011]
M35003-4	NA1299	Atl N	1299 m	*C. wuellerstorfi*	*Hüls and Zahn* [2000]
				Cibicidoides kullenbergi	*Zahn and Stüber* [2002]
				Cibicidoides pseudoungerianus	*Rühlemann et al.* [1999]
MD07-3076Q	SA3770	Atl S	3770 m	*C. kullenbergi*	*Waelbroeck et al.* [2011]
					Skinner et al. [2010]
MD98-2165	EI2100	Ind E	2100 m	*C. wuellerstorfi*	*Waelbroeck et al.* [2006]
				Cibicidoides spp.	
MD99-2334K	NA3146	Atl N	3146 m	*Planulina wuellerstorfi*	*Skinner and Shackleton* [2004]
				Globobulimina affinis	*Skinner et al.* [2003]
NIOP-905	NI1580	Ind N	1580 m	*C. kullenbergi*	*Jung et al.* [2001]
				Cibicidoides spp.	*Jung et al.* [2009]
					Ivanochko et al. [2005]
TR163-31b	EP3210	Pac E	3210 m	*Uvigerina senticosa*	*Shackleton et al.* [1988]
				C. wuellerstorfi	*Skinner and Shackleton* [2005]

[a]"Code" indicates reference codes used in this paper for ease of discussion. SA1967 refers to a South Atlantic core at 1967 m depth, NI1580 to a North Indian core at 1580 m depth, etc. All species are from the genus *Cibicidoides* except for cores NA3146 (*Planulina* and *Globobulimina*) and EP3210 (*Uvigerina*).

but SA3770 come from continental margins, and all but two are based on tests from the genus *Cibicidoides*; $\delta^{18}O_c$ records for cores NA3146 and EP3210 are derived at least in part from other genera.

Chronologies of benthic $\delta^{18}O_c$ records were derived primarily from radiocarbon ages of planktonic foraminifera extracted from the same sediment core. For all records but two (SA1967 and NA1299) the published age models are used in this study. In SA1967 and NA1299 the published age models were constrained in part by tuning those records to benthic $\delta^{18}O_c$ from other sediment cores; new age models for those cores were constructed by computing calendar ages from published ^{14}C ages using OxCal 4.1 [*Bronk Ramsey*, 2009; *Reimer et al.*, 2009] and linearly interpolating between ^{14}C-derived ages with depth. Previously published age models for NA3146 and NA3223 used in this study rely in part on synchronization of planktonic $\delta^{18}O_c$

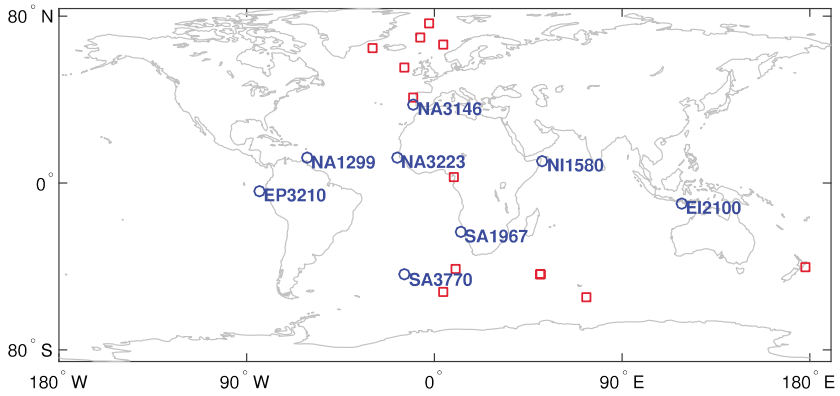

Figure 1. Locations of the eight benthic (blue, with labels) and 13 planktonic (red squares) records of $\delta^{18}O_c$ used in this study. Locations and names of planktonic records are listed in Table 2.

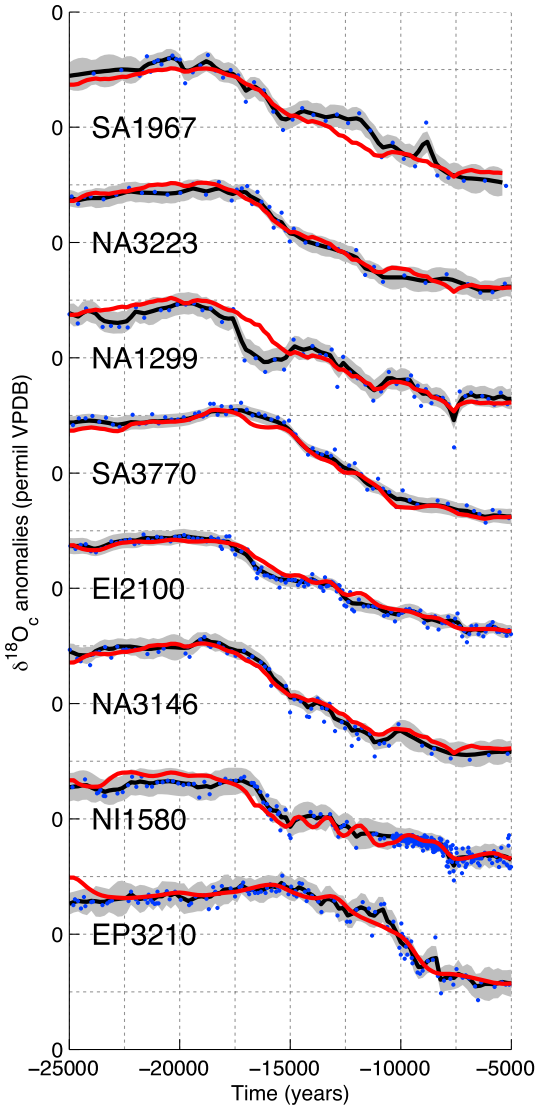

Figure 2. Eight benthic foraminiferal $\delta^{18}O_c$ anomaly records are used to infer ML conditions. Blue dots show the published data, the solid black line their objectively mapped values, and the gray shading the objectively mapped one-sigma uncertainty. Red lines show the reconstructed data, $\tilde{\mathbf{y}}^*$, (see text) derived from the ML $\delta^{18}O_c$ solution obtained in section 4 with the small effect due to initial conditions added back. Vertical grid spacing is 1‰, and record order is arbitrary.

records derived from those cores to planktonic $\delta^{18}O_c$ records for cores SU81-18 [*Bard et al.*, 1987] and MD95-2042 [*Shackleton et al.*, 2004], respectively.

Each benthic $\delta^{18}O$ record shows a deglacial decrease of 1–2‰ over the interval from 25 to 5 ka, but the timing of these transitions appears asynchronous with the age models used (Figure 2). The deglacial $\delta^{18}O_c$ decrease in core EP3210 begins at roughly 15 ka, markedly later than in other records. Records at shallower depths (NI1580, EI2100, SA1967, and NA1299) appear to share a two-stage decrease in $\delta^{18}O$, with the first transition occurring between roughly 18 ka and 16 ka.

Only temporal anomalies relative to each sediment core record's time mean are considered in this paper. Subtraction of record time means mitigates effects of interlaboratory and interspecies $\delta^{18}O_c$ offsets [e.g., *Ostermann and Curry*, 2000] as well as a small nonconservative effect due to pressure. Isolation of record anomalies is permitted by the linearity of passive tracer transport; in solving the inverse problem using the anomalies, it is assumed that record means, anomalies, and their respective uncertainties are uncorrelated. The separate inverse problem of finding a history of ML $\delta^{18}O_c$ satisfying the record time means is ignored because record means are biased from true means by finite record lengths.

Benthic $\delta^{18}O_c$ anomaly records may be decomposed into "signal" and "noise" components, where the signal is the true in situ $\delta^{18}O_c$ and the noise consists of supposedly random variations due to observational and representational errors. Signal and noise are both assumed to be Gaussian processes. Explicit noise statistics are required to use the data quantitatively; here, following *LeGrand and Wunsch* [1995], *Gebbie and Huybers* [2006], and *Marchal and Curry* [2008], observational errors are described by zero mean white noise with standard deviation $\sigma_n = 0.2$‰.

Due to variable sampling procedures and sedimentation rates, measurements within each benthic $\delta^{18}O_c$ record are spaced irregularly in time. To avoid preferential fits in the least-squares procedure to benthic records during densely sampled time periods, objective mapping [e.g., *Bretherton et al.*, 1976; *Wunsch*, 2006] is used to generate time series that are regularly spaced at 200 year intervals spanning 25 ka to 5 ka (Figure 2). To compute objectively mapped values, a statistically stationary estimate of the signal autocovariance, $R(\tau) = \langle s(t)s(t-\tau)\rangle$, is necessary for each record, where τ is a time lag, s is the $\delta^{18}O_c$ record signal component, and angle brackets indicate the expected value. Signal autocovariances are calculated by fitting a power law to the structure function, $V(\tau) \equiv \frac{1}{2}\left\langle [s(t+\tau) - s(t)]^2 \right\rangle = \left\langle s^2(t)\right\rangle - R(\tau)$, computed between every two points in each record [*Press et al.*, 1992; *Rybicki and Press*, 1992; *Amrhein*, 2014]; the signal variance, $\left\langle s^2(t)\right\rangle$, is approximated from the record variances and σ_n. The resulting interpolation (Figure 2) has uncertainties determined

Table 2. Summary of Planktonic Foraminiferal $\delta^{18}O_c$ Records[a]

Core	Latitude	Longitude	Species	References
MD03-2707	2.5°N	9.4°E	*G. Ruber*	*Weldeab et al.* [2007]
PS1906-2	76.8°N	2.2°W	*N. pachy s.*	*Nees and Thiede* [1993]
PS1243-1	69.4°N	6.6°W	*N. pachy* s.	*Bauch et al.* [2001]
MD95-2010	66.7°N	4.6°E	*N. pachy* s.	*Dokken and Jansen* [1999]
GIK23519-5	64.8°N	29.6°W	*N. pachy* s.	*Millo et al.* [2006]
P69	40.4°S	178°E	*G. bulloides*	*Nelson et al.* [2000]
ODP177-1089	40.9°S	9.9°E	*G. bulloides*	*Hodell et al.* [2003]
MD73-025	43.5°S	51.2°E	*N. pachy* s.	*Labracherie et al.* [1989]
MD84-527	43.5°S	51.2°E	*N. pachy* s.	*Pichon et al.* [1992]
RC13-271	52.0°S	4.5°E	*N. pachy* s./d.	*Charles et al.* [1991]
MD84-551	55°S	73.2°E	*N. pachy* s.	*Pichon et al.* [1992]
MD95-2040	40.6°N	10.1°W	*G. bulloides*	*Schönfeld et al.* [2003]
ODP980	55.5°N	14.7°W	*N. pachy* s.	D. Oppo and J. McManus (personal communication, 2014)

[a]"*N.*" and "*G.*" stand for *Neogloboquadrina* and *Globigerina*; "pachy" stands for pachyderma; and "s." and "d." stand for sinistral and dextral.

by σ_n, the estimate of $R(\tau)$, and the data distribution. Because objectively mapped values are linear combinations of observations, uncertainty is autocorrelated in time within each record. Uncertainty is assumed to be uncorrelated between records because observational and representational error processes at distant core sites are likely to be independent.

Thirteen planktonic $\delta^{18}O_c$ records (Figure 6 and Table 2) were selected on the basis of resolution, presence of ^{14}C-derived age models, duration, and location in the North Atlantic or Southern Oceans (section 4). Eight records were derived from *Neogloboquadrina pachyderma* (sinistral), three from *Globigerina bulloides*, one from G. ruber, and one from *N. pachyderma* (both sinistral and dextral). Original published age models are used. All age models are derived from ^{14}C dates on planktonic foraminifera and (or) by correlation to ice core records, with the caveat that several models may not include updated ^{14}C reservoir ages [e.g., *Skinner et al.*, 2010]. Each record has a glacial-interglacial transition of 1–2‰. Spatial variations among planktonic $\delta^{18}O_c$ records are due to local and regional variability as well as record noise.

3. Model-data Analysis

3.1. Relating Benthic Proxies to ML Conditions

A tracer transport model is used to relate sediment core benthic $\delta^{18}O_c$ records to mixed layer $\delta^{18}O_c$ histories. Similar to *Lund et al.* [2011], the procedure treats $\delta^{18}O_c$ as conservative everywhere, except for source contributions in the ML. Experimental studies [e. g., *Bemis et al.*, 1998] show that $\delta^{18}O_c$ measured on foraminifera is well represented by a linear function of seawater $\delta^{18}O$, $\delta^{18}O_w$, and temperature, T. Nonconservative pressure effects on T yield biases of 0.02–0.07‰ for each core depending on depth and latitude [*Fofonoff and Millard*, 1983; *Bryden*, 1973; *Saunders*, 1981]. This effect is mitigated by the subtraction of record means and is otherwise neglected.

To illustrate the data analysis method generically, define first a state vector, $\mathbf{c}(t) = \left[c_1(t), c_2(t), \ldots c_N(t)\right]^\top$, where $c_i(t)$ is $\delta^{18}O_c$ at a time t in the ith of N grid boxes subdividing the ocean domain below the ML. Likewise define the vector $\mathbf{q}(t) = \left[q_1(t), q_2(t), \ldots q_L(t)\right]^\top$ to be the $\delta^{18}O_c$ in L ML regions. Evolution of the state vector is written in the canonical form

$$\mathbf{c}(t + \Delta t) = \mathbf{A}\mathbf{c}(t) + \mathbf{F}\mathbf{q}(t). \quad (1)$$

Lower case and upper case bold variables are vectors and matrices, respectively. The matrix **A** is the so-called state transition matrix, and **F** describes the influence of $\mathbf{q}(t)$ on the state at the time $t + \Delta t$ [*Wunsch*, 2006]. Here we assume (from the null hypothesis) that **A** and **F** are steady and known from the modern circulation.

Define $\mathbf{y}(t) = \left[y_1(t), y_2(t), \ldots y_M(t)\right]^\top$ to be the objectively mapped benthic $\delta^{18}O_c$ anomalies (section 2) from M sediment cores, and let $\mathbf{n}(t) = \left[n_1(t), n_2(t), \ldots n_M(t)\right]^\top$ be the errors in those anomalies. Benthic $\delta^{18}O_c$ anomalies are expressed as noisy measurements of the model state, $\mathbf{c}(t)$,

$$\mathbf{y}(t) = \mathbf{B}\mathbf{c}(t) + \mathbf{n}(t), \tag{2}$$

where the matrix $\mathbf{B}$ relates benthic $\delta^{18}O_c$ anomalies at sediment core locations to $\delta^{18}O_c$ at the nearest grid boxes. Offsets of 200–300 m exist in several cases between model grid box centers and core depths, effects of which are not considered.

To write a single matrix equation relating the time history of ML $\delta^{18}O_c$ to benthic observations at all times, define concatenated vectors of values ordered first in space and then in time as underlined vectors,

$$\underline{\mathbf{y}} = \left[\mathbf{y}(t_0)^\top, \mathbf{y}\left(t_0 + 1\Delta t\right)^\top, \ldots, \mathbf{y}\left(t_0 + S\Delta t\right)^\top\right]^\top \tag{3}$$

$$\underline{\mathbf{n}} = \left[\mathbf{n}(t_0)^\top, \mathbf{n}\left(t_0 + 1\Delta t\right)^\top, \ldots, \mathbf{n}\left(t_0 + S\Delta t\right)^\top\right]^\top \tag{4}$$

$$\underline{\mathbf{q}} = \left[\mathbf{q}(t_0)^\top, \mathbf{q}\left(t_0 + 1\Delta t\right)^\top, \ldots, \mathbf{q}\left(t_0 + S\Delta t\right)^\top\right]^\top, \tag{5}$$

where $S+1$ is the number of times when observations are present and t_0 is the initial such time. The initial conditions, data, noise, and ML conditions are related by

$$\underline{\mathbf{y}} = \underline{\mathbf{y}}_0 + \underline{\mathbf{G}}\underline{\mathbf{q}} + \underline{\mathbf{n}}, \tag{6}$$

where the matrix $\underline{\mathbf{G}}$ is described in Appendix A and $\underline{\mathbf{y}}_0$ is the contribution due to initial conditions, which decays to 0 after 5000 years in the present problem. As it is not the focus of this study, $\underline{\mathbf{y}}_0$ is estimated separately as $\underline{\tilde{\mathbf{y}}}_0$ (not shown) by forward propagating a least-squares fit of time-constant ML $\delta^{18}O_c$ to benthic anomalies averaged over −25,000 to −20,000 years. Defining $\underline{\mathbf{y}}^* = \underline{\mathbf{y}} - \underline{\tilde{\mathbf{y}}}_0$ and ignoring uncertainties in the estimation of $\underline{\tilde{\mathbf{y}}}_0$, the observations and ML conditions at all times are related by

$$\underline{\mathbf{y}}^* = \underline{\mathbf{G}}\underline{\mathbf{q}} + \underline{\mathbf{n}}. \tag{7}$$

This equation is solved to estimate the history of ML $\delta^{18}O_c$ ($\underline{\mathbf{q}}$) from benthic $\delta^{18}O_c$ anomalies ($\underline{\mathbf{y}}^*$) in the presence of a modern ocean circulation model ($\underline{\mathbf{G}}$) and record noise ($\underline{\mathbf{n}}$).

The matrix $\underline{\mathbf{G}}$ is constructed from adjoint Green's functions, which are computed by integrating a circulation model backward in time for 5000 years under Heaviside conditions at each grid box representing a $\delta^{18}O_c$ record (i.e., at each of those grid boxes, $c(t) = 0$ for $t < 0$ and $c(t) = 1$ for $t \geq 0$, with $c(t) = 0$ at all other grid boxes and times) and differencing the output in time. Contributions after 5000 years are set to 0, which is accurate to within 10^{-5}. The present approach is closely related to applications using transit time distributions, which are a form of Green's function [*Peacock and Maltrud*, 2006; *Rutberg and Peacock*, 2006].

The model used is a statistically steady state representation of the combined effects of advection and mixing in the modern ocean circulation [*Gebbie and Huybers*, 2010, 2012, hereafter GH12]. Transports calculated in an ocean general circulation model (GCM) could also be used for this purpose; the GH12 model was chosen for its abilities to represent tracer distributions in the modern ocean and to approximate regions and rates of deepwater formation, which are poorly simulated in most GCMs. The GH12 circulation was estimated using observations of potential temperature, salinity, phosphate, nitrate, and oxygen from a hydrographic compilation (World Ocean Circulation Experiment and previous measurements, *Gouretski and Koltermann* [2004]), a gridded seawater $\delta^{18}O$ product [*LeGrande and Schmidt*, 2006], and the Global Data Analysis Project gridded data set of prebomb radiocarbon [*Rubin and Key*, 2002; *Key et al.*, 2004]. The model domain has 33 vertical levels and a $4^\circ \times 4^\circ$ resolution with $L = 2806$ ML regions whose vertical extent is defined using modern observed winter ML depth [*Conkright et al.*, 1994].

Figure 3 shows the adjoint Green's functions for cores EP3210 and NA3146. The method of empirical orthogonal functions [e.g., *Preisendorfer and Mobley*, 1988] was used to plot each adjoint Green's function as a single spatial pattern varying in time; in both cases this approximation captures more than 90% of the total spatiotemporal variance. The adjoint Green's functions show that tracer propagation to core sites smooths ML

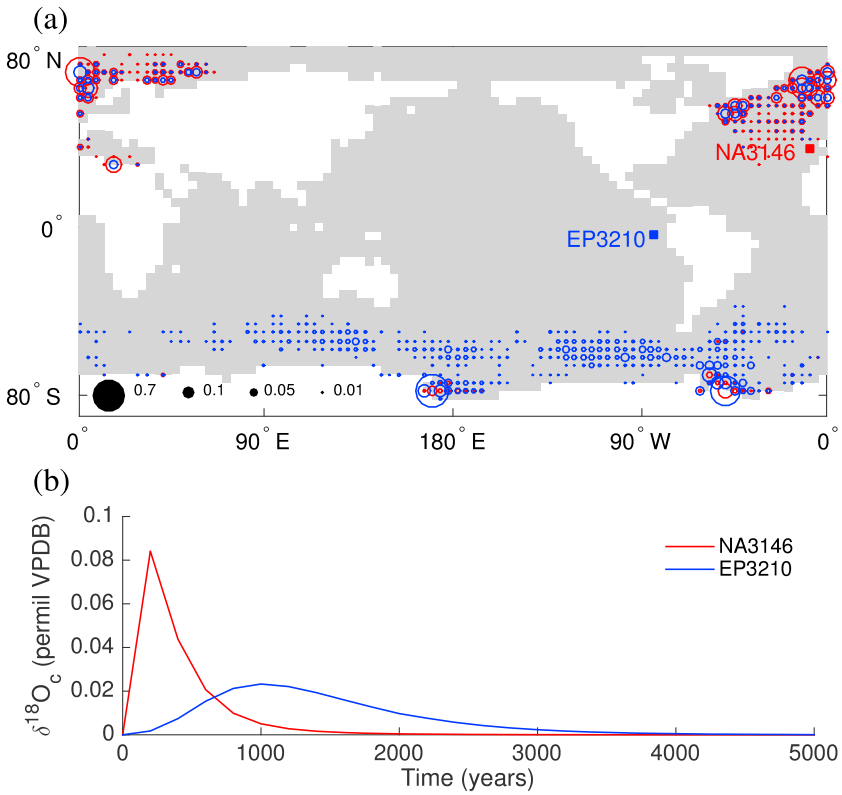

Figure 3. Adjoint Green's functions for NA3146 (red, Iberian Margin) and EP3210 (blue, eastern equatorial Pacific) computed using the GH12 model (see text). The adjoint Green's functions may be interpreted as follows. In the case when ML $\delta^{18}O_c$ conditions are a delta function in the *i*th ML grid box at $t = 0$ (that is, $q_i(t) = 1‰$ at $t = 0$ and $q(t) = 0‰$ at all other places and times), the signal at each deep core site as the model is integrated forward in time is equal to (b) the time trajectory, scaled by the fraction indicated by (a) the circled area in the *i*th grid box. Where there are no circles, the tracer communicated to core sites is very small or 0. An approximation is made in representing the adjoint Green's functions by a pair of spatial and temporal patterns (see text); over 90% of the variability is accounted for at both core sites.

tracer anomalies in time and that outside of model high latitudes, tracer signals are minimally communicated to core sites. The adjoint Green's function is broader in time for the deep Pacific core site than for the deep North Atlantic core site, qualitatively consistent with longer tracer equilibration time in basins far from deepwater formation regions [*Wunsch and Heimbach*, 2008]. The NA3146 site is bathed primarily in deep water formed in the North Atlantic and Arctic, whereas the EP3210 site is mostly influenced by Southern Ocean waters.

The model time step used is $\Delta t = 200$ years, the initial time is $t_0 = -25{,}000$ years, and the number of time steps is 101, corresponding to reconstruction dates $t = -25{,}000, -24{,}800, \ldots -5000$ years. The data and noise, $\underline{\mathbf{y}}^*$ and $\underline{\mathbf{n}}$, are each 806 × 1 vectors whose length equals the total number of objectively mapped observations, and $\underline{\mathbf{q}}$ is a 283,406 × 1 vector whose length corresponds to the number of ML regions (2806) at every time (101) in the reconstruction. In total, 283,406 unknown ML $\delta^{18}O_c$ values and 806 unknown observational errors are constrained by 806 objectively mapped benthic $\delta^{18}O_c$ anomalies.

3.2. Solution Method for Benthic-Derived ML $\delta^{18}O_c$

The singular value decomposition (SVD) [e. g., *Wunsch*, 2006] is used to find solutions for $\underline{\mathbf{q}}$ in equation (7). The SVD of $\underline{\mathbf{G}}$ is $\underline{\mathbf{G}} = \mathbf{U}\mathbf{\Lambda}\mathbf{V}^{\mathrm{T}}$, where $\mathbf{U}$ and $\mathbf{V}$ are square orthonormal matrices and $\mathbf{\Lambda}$ is a nonsquare diagonal matrix with K strictly positive singular values $\lambda_1, \lambda_2, \ldots \lambda_K$ in decreasing order along the diagonal. The *i*th columns of $\mathbf{U}$ and $\mathbf{V}$ (the singular vectors) are written as $\mathbf{u}_i$ and $\mathbf{v}_i$, respectively. Denoting estimated values with a tilde, the general solution for $\underline{\mathbf{q}}$ computed by SVD is

$$\underline{\tilde{\mathbf{q}}} = \sum_{i=1}^{K'} \frac{\mathbf{u}_i^{\mathrm{T}} \underline{\mathbf{y}}^*}{\lambda_i} \mathbf{v}_i + \sum_{i=K'+1}^{283406} \alpha_i \mathbf{v}_i. \tag{8}$$

In the solution, the first K' of the $\mathbf{v}_i$ (the effective range vectors) are weighted by the projection of the data, $\underline{\mathbf{y}}^*$, onto the corresponding $\mathbf{u}_i$ and inversely weighted by λ_i. The remaining $\mathbf{v}_i$ (the effective null-space vectors) are weighted by unknown coefficients α_i, all of which are set to 0, yielding the so-called truncated SVD solution. The effective rank, $K' \leq K$, specifies the number of singular vectors retained in the solution (the effective range vectors) and is chosen based on the singular values, whose magnitudes are very low when data sparsity and (or) noise precludes resolving the corresponding vectors.

Quantification of solution uncertainties is essential to compare benthic-derived ML $\delta^{18}O_c$ to planktonic records. The truncated SVD solution uncertainty matrix, $\mathbf{P}$, describes the expected squared deviation of estimated ML $\delta^{18}O_c$ from the true values [*Wunsch*, 2006],

$$\mathbf{P} = \left\langle \left(\underline{\tilde{\mathbf{q}}} - \underline{\mathbf{q}}\right)\left(\underline{\tilde{\mathbf{q}}} - \underline{\mathbf{q}}\right)^{\top} \right\rangle = \sum_{i=1}^{K'}\sum_{j=1}^{K'} \mathbf{v}_i \frac{\mathbf{u}_i^{\top}\left\langle \underline{\mathbf{n}}\underline{\mathbf{n}}^{\top}\right\rangle \mathbf{u}_j}{\lambda_i \lambda_j}\mathbf{v}_j^{\top} + \sum_{i=K'+1}^{283406}\sum_{j=K'+1}^{283406} \mathbf{v}_i \left\langle \alpha_i \alpha_j \right\rangle \mathbf{v}_j^{\top}. \tag{9}$$

Define the two components of $\mathbf{P}$ to be $\mathbf{P}_c$ and $\mathbf{P}_{\text{null}}$, respectively. The solution covariance, $\mathbf{P}_c$, describes uncertainty due to the observational error covariance, $\left\langle \underline{\mathbf{n}}\underline{\mathbf{n}}^{\top}\right\rangle$, (estimated by objective mapping in section 2); the square root of its diagonal elements is the solution standard error. The contribution to the solution standard error from including the ith singular vector is proportional to $1/\lambda_i^2$, indicating that $\mathbf{P}_c$ is highly sensitive to small values of λ_i. The null-space uncertainty, $\mathbf{P}_{\text{null}}$, describes uncertainty from null-space vectors. A tradeoff exists in choosing K': as $K' \rightarrow K$, $\mathbf{P}_{\text{null}}$ grows smaller as the number of effective null-space vectors decreases, but $\mathbf{P}_c$ grows larger as small λ_i are included in $\underline{\tilde{\mathbf{q}}}$. Here K' is chosen based on the λ_i with the goal of minimizing the total solution uncertainty.

The solution covariance, $\mathbf{P}_c$, is readily computed from the SVD and $\left\langle \underline{\mathbf{n}}\underline{\mathbf{n}}^{\top}\right\rangle$, but additional a priori information about the null-space weights, α_i, is required for an absolute estimate of $\mathbf{P}_{\text{null}}$. Instead, a relative measure of $\mathbf{P}_{\text{null}}$ is given by the solution resolution matrix, $\mathbf{T}_v$,

$$\mathbf{T}_v = \mathbf{V}_{K'}\mathbf{V}_{K'}^{\top}, \tag{10}$$

where $\mathbf{V}_{K'} = \left[\mathbf{v}_1, \ldots \mathbf{v}_{K'}\right]$ is the semiorthogonal matrix of right singular vectors in the effective range of $\underline{\mathbf{G}}$. The solution resolution matrix relates inferred and true ML $\delta^{18}O_c$,

$$\underline{\tilde{\mathbf{q}}} = \mathbf{T}_v \underline{\mathbf{q}}, \tag{11}$$

in the absence of observational uncertainty and illustrates which features of $\underline{\mathbf{q}}$ lie in the null space and cannot be reproduced in $\underline{\tilde{\mathbf{q}}}$ [*Wunsch*, 2006]. In the benthic tracer inverse problem, unresolvable features in time are due to low-pass filtering by ocean tracer propagation [*Rutberg and Peacock*, 2006; *Amrhein*, 2014], and unresolvable features in space are due to the sparsity of deepwater formation regions and mixing in the ocean interior (section 4 and Appendix C).

The pointwise resolvability, r, is derived from $\mathbf{T}_v$ and describes the spatial distribution of $\mathbf{P}_{\text{null}}$, which is important for comparing $\underline{\tilde{\mathbf{q}}}$ to planktonic records. To define r, consider the hypothetical scenario where the true ML $\delta^{18}O_c$ deglacial history, $\underline{\mathbf{q}}_{\text{hyp},i}$, is q_0 in the ith ML grid box and 0‰ everywhere else at all times over the last deglaciation. By equation (11), the reconstructed ML $\delta^{18}O_c$ is $\underline{\tilde{\mathbf{q}}}_{\text{hyp},i} = \mathbf{T}_v\underline{\mathbf{q}}_{\text{hyp},i}$. Let $\tilde{q}_0$ be the deglacial time mean value of the ith grid box element in $\underline{\tilde{\mathbf{q}}}_{\text{hyp},i}$. The pointwise resolvability is defined as

$$r_i = \frac{\tilde{q}_0}{q_0}, \quad 0 \leq r_i \leq 1 \tag{12}$$

and indicates what fraction of a ML $\delta^{18}O_c$ signal in the ith grid box on the longest time scale will be reconstructed at the same location by the particular SVD solution. Insofar as ocean tracer transport acts as a low-pass filter, r serves as an upper limit on the resolvability of shorter-timescale variability.

An additional diagnostic afforded by the SVD solution is the data resolution matrix,

$$\mathbf{T}_u = \mathbf{U}_{K'}\mathbf{U}_{K'}^{\top}, \tag{13}$$

where $\mathbf{U}_{K'} = \left[\mathbf{u}_1, \ldots \mathbf{u}_{K'}\right]$ is the semiorthogonal matrix of left singular vectors in the effective range of $\underline{\mathbf{G}}$. The diagonal elements of $\mathbf{T}_u$ are the "data importance" and describe the relative importance of each observation in determining the solution [*Wunsch*, 2006].

Before computing the SVD, the problem is weighted to reflect observational uncertainty (derived from objective mapping, section 2) and scaled by the column norms of $\underline{\mathbf{G}}$ [*Wunsch*, 2006] to remove biases from spatial variations in vertical transport out of the ML, at the expense of introducing covariance between solution elements (Appendix C). Of the 283,406 singular values of $\underline{\mathbf{G}}$, $K = 806$ are nonzero, corresponding to the number of objectively mapped observations at all times. Section 4 discusses results using $K' = 230$, chosen so that singular values less than the typical standard deviation of the objectively mapped observational noise lie in the null space. Larger values of K' improve the fit to the data (up to an exact fit for $K' = 806$), at the expense of rapidly increasing solution amplitudes and standard errors. Smaller values of K' yield inferior fits to the observations.

3.3. Relating Planktonic Proxies to ML Conditions

Planktonic $\delta^{18}O_c$ observations (section 2, written for all locations and times as the underlined vector $\underline{\mathbf{y}}^p$) and $\underline{\mathbf{q}}$ can be related in a generic linear form as

$$\underline{\mathbf{y}}^p = \underline{\mathbf{R}}\underline{\mathbf{q}} + \underline{\mathbf{n}}^p, \tag{14}$$

where $\underline{\mathbf{R}}$ is a matrix describing which ML regions and times are constrained by planktonic observations (analogous to $\underline{\mathbf{G}}$ for benthic records) and $\underline{\mathbf{n}}^p$ is the planktonic observational noise. Planktonic-derived ML $\delta^{18}O_c$ estimates are written as $\underline{\tilde{\mathbf{q}}}^p$. Ideally, the matrix $\underline{\mathbf{R}}$ should represent plankton vital effects as well as covariances between $\delta^{18}O_c$ in the ML and planktonic habitats, but these processes are poorly understood. Here the simplifying assumption is made that planktonic records measure $\delta^{18}O_c$ in the ML overlying their sediment core site; uncertainties in this representation are not assessed.

4. Results

4.1. ML $\delta^{18}O_c$ Inferred From Benthic Data

The truncated SVD solution, $\underline{\tilde{\mathbf{q}}}$, to equation (7) is a deglacial time history of ML $\delta^{18}O_c$ for all ML locations at $t = -25{,}000, -24{,}800, \ldots -5000$ years derived from eight benthic $\delta^{18}O_c$ records. Null-space uncertainties place strong limits on reconstruction fidelity, as diagnosed by the pointwise resolvability (Figure 4), which is nonuniformly distributed and generally small ($r < 0.01$) outside of high latitudes. Low r values imply that (1) only a small fraction of the true variability in each ML region is reconstructed and that (2) many other candidate solutions will fit the benthic data equally well. Evidently, in the context of the modern circulation, the benthic records effectively carry no information about the evolution of deglacial ML $\delta^{18}O_c$ outside of high latitudes. Understanding how high-latitude ML $\delta^{18}O_c$ covaried with values in other regions might permit benthic records to constrain those regions as well (section 5).

The spatial distribution of pointwise resolvability is similar to that of the adjoint Green's functions (Figure 3), which in turn reflect dominant "ocean-filling" sites in the GH12 model [*Gebbie and Huybers*, 2011]. Clearly, only $\delta^{18}O_c$ in ML regions that play a large role in ventilating the deep ocean can be reconstructed with any fidelity; the rationale is that only those regions have contributions to $\delta^{18}O_c$ at core sites that are not dwarfed by observational noise. Appendix C demonstrates this tendency in a four-box model. As different modeled circulations have different surface regions that are most important for filling the deep ocean, the pointwise resolvability is sensitive to the steady circulation that is assumed.

Figure 4 plots $\underline{\tilde{\mathbf{q}}}$ as time series in five regions with nonzero r. All regions show glacial-interglacial transitions of 1–2‰ superimposed upon several qualitatively different patterns of millennial and multimillennial variability. Regions not plotted also have 1–2‰ deglacial transitions, with similar patterns of variability, except for regions lying in the solution null space, where the reconstructed value is 0‰. Examination of $\mathbf{P}_c$ (not shown) reveals that coherences within and between regions are highly uncertain and are likely due to data sparsity, as there is insufficient information to "unmix" contributions of different ML grid boxes to benthic core sites and to resolve spatial gradients in ML $\delta^{18}O_c$, so that spatially broad patterns are inferred (demonstrated in a four-box model in Appendix C). The standard error (not shown) in ML $\delta^{18}O_c$ is between 0‰ and 0.6‰ at each time and location; in general, grid boxes with small pointwise resolvabilities have small standard errors because uncertainties in the data project minimally onto regions that are poorly constrained by the data. Together, the solution and pointwise resolvability suggest that the benthic data are able (weakly) to resolve weighted spatial averages of ML $\delta^{18}O_c$ in regions of deepwater formation, as well as grid-scale variability at locations whose contributions to ventilating the deep ocean in the model of GH12 are exceptionally high.

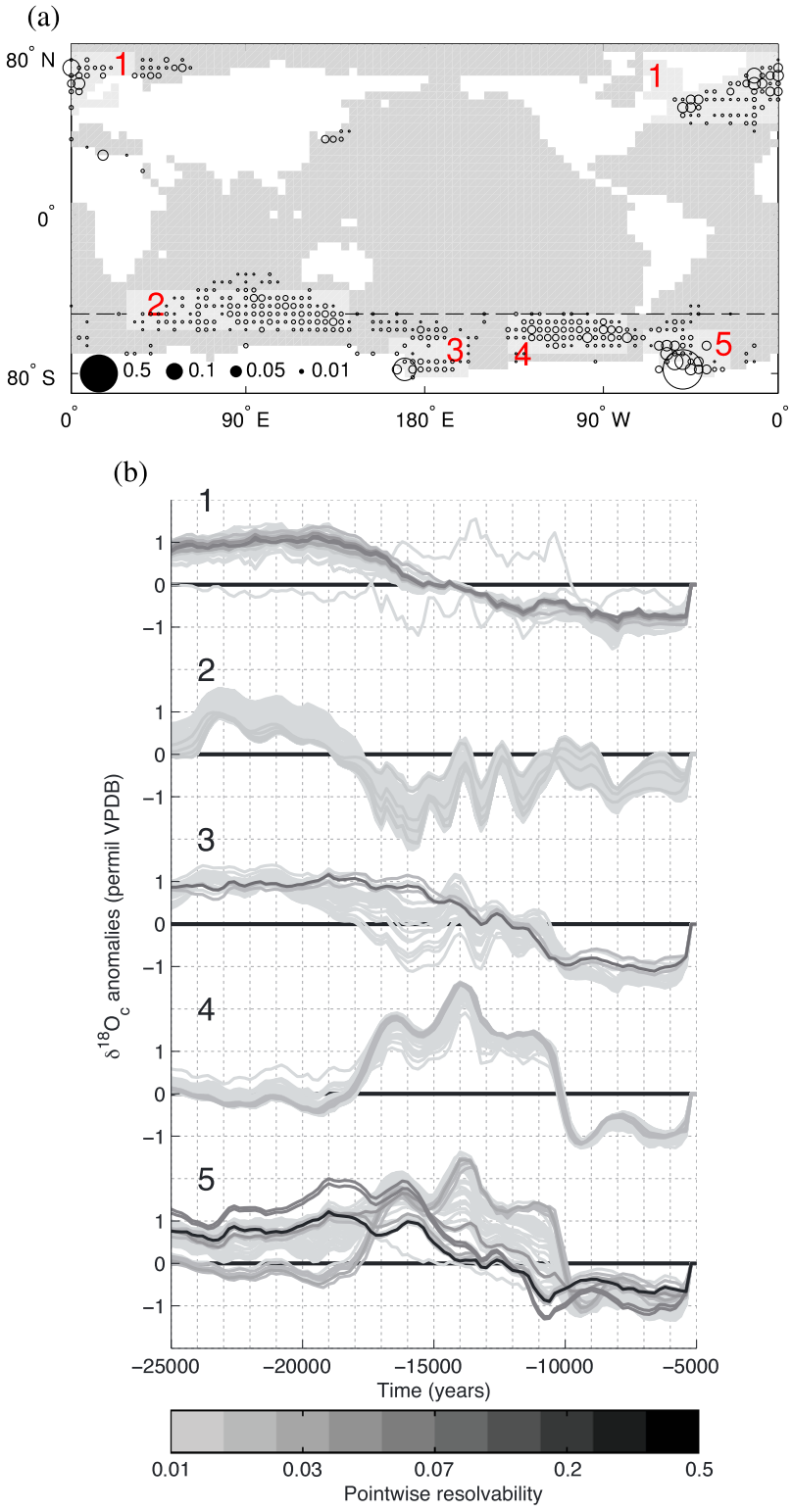

Figure 4. (a) Circle area indicates the pointwise resolvability r for the underlying grid box; filled circles over land in the lower left provide a legend. Locations without circles have resolvability < 0.01. Lighter gray areas define regions plotted in (b). Box 1 and the region south of the dotted line at 50°S are averaged to compute the North Atlantic and Southern Ocean time series $\tilde{m}_{NA}$ and $\tilde{m}_{SO}$, respectively (see text). (b) The solution $\bar{\mathbf{q}}$ plotted as overlaid time series at every grid box within the five geographical regions and shaded by pointwise resolvability. In all regions, values after 6 ka lie in the null space and are equal to 0, as they are not constrained by objectively mapped benthic observations, which end at 5 ka. Note the nonlinear color bar.

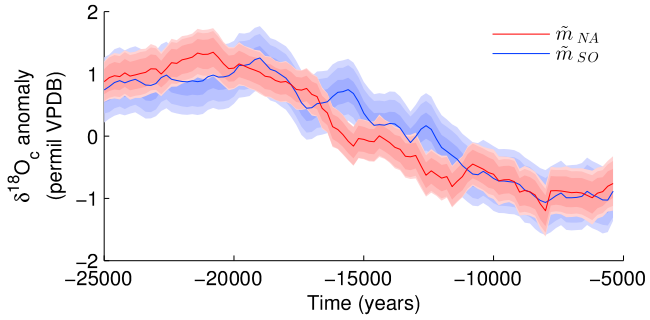

Figure 5. Estimates of ML $\delta^{18}O_c$ anomalies in the North Atlantic ($\tilde{m}_{NA}$) and Southern Oceans ($\tilde{m}_{SO}$) derived from benthic records. The inner error bar is the standard error, the middle envelope includes the null-space contribution when ML $\delta^{18}O_c$ is assumed hemispherically covarying, and the outer envelope includes the null-space contribution when ML $\delta^{18}O_c$ is assumed spatially uncorrelated (see text).

The reconstructed data, $\tilde{\mathbf{y}}^* = \mathbf{G}\tilde{\mathbf{q}}$, is the $\delta^{18}O_c$ reconstructed at benthic core locations when ML conditions are $\tilde{\mathbf{q}}$ in an integration of the GH12 model over the deglaciation. Many characteristics of the data are reconstructed in $\tilde{\mathbf{y}}^*$ (Figure 2): a deglacial transition of plausible amplitude is evident at every core site, no biases are apparent, and many record features are recovered. The reconstruction of a last deglacial ML $\delta^{18}O_c$ history assuming the modern circulation that largely agrees with eight benthic records is not a trivial result. If such a history could not be found, then one might conclude that the misfit was due to a deviation from the modern circulation. The misfit to NA1299 during 18–16 ka can be reduced by choosing $K' = 500$, at the expense of introducing high-amplitude, millennial-scale variability and large standard errors to the solution in the Southern Hemisphere; even larger values of K' are necessary to reduce the misfit to SA1967 during 15–13 ka.

Spatially averaged time series of $\tilde{\mathbf{q}}$ computed for the North Atlantic ($\tilde{m}_{NA}(t)$) and the Southern Ocean ($\tilde{m}_{SO}(t)$) are shown in Figure 5 (corresponding regions are shown in Figure 4; Appendix B describes the mean estimation procedure). Null-space uncertainties are computed using two examples of possible covariance matrices $\left\langle \mathbf{qq}^{\mathrm{T}} \right\rangle$; both assume that $\mathbf{q}$ is Gaussian with zero mean and standard deviation equal to 1‰, with no autocorrelation in time. In the first example, no spatial covariance is imposed between ML grid boxes, and in the second example, ML $\delta^{18}O_c$ is made to be spatially uniform within the Northern and Southern Hemispheres. Both cases likely underestimate the true null-space uncertainty.

Both $\tilde{m}_{NA}(t)$ and $\tilde{m}_{SO}(t)$ have maximum values of $\delta^{18}O_c$ between 21 and 19 ka and minimum values at 8 ka, and solution variances are dominated by a roughly 2‰ glacial-interglacial transition. On the interval from 17 ka to 11 ka, $\tilde{m}_{NA}(t)$ is persistently less than $\tilde{m}_{SO}(t)$, with the largest differences (0.8‰ and 0.7‰) centered on 15.6 ka and 12.6 ka. Uncertainty contributions due to $\mathbf{P}_c$ and $\mathbf{P}_{null}$ are comparable in size, and null-space uncertainties are smaller when $\mathbf{q}$ is assumed spatially uniform within hemispheres. It is tempting to speculate about causes for interhemispheric variability in the inferred ML $\delta^{18}O_c$, but given the large uncertainties, differences between $\tilde{m}_{NA}(t)$ and $\tilde{m}_{SO}(t)$ are not significantly different from 0‰.

Because ML $\delta^{18}O_c$ histories are poorly constrained by benthic records, additional prior constraints on the solution could change its character substantially and reduce biases from the true solution. For instance, consideration of temperature and $\delta^{18}O_w$ suggests that inferred $\delta^{18}O_c$ values (Figure 4) in the Southern Ocean (SO) are biased high at the Last Glacial Maximum (LGM, approximately 23–19 ka). Given the inferred LGM-Holocene anomaly of $\Delta\delta^{18}O_c = 2.25$‰ (Figure 5), using a paleotemperature equation [*Bemis et al.*, 1998], $\delta^{18}O_c = 3.4 + \delta^{18}O_w - 0.21T$, and attributing 1‰ to global ice volume differences from pore water measurements [*Adkins et al.*, 2002], LGM average SO ML temperatures are inferred to be 6°C lower than in the Holocene, lower than the freezing point in much of the modern SO ML. (The effect of roughly 1g/kg higher global average salinities at the LGM on the freezing point of water is a depression of roughly 0.06°C [*McDougall and Barker*, 2011], too small to compensate for the inferred deviation.) For several reasons ($\Delta\delta^{18}O_c$ has a large uncertainty; local patterns of warming and cooling within the SO are possible; and porewater-derived glacial $\delta^{18}O_w$ may not be representative of the SO ML), we do not reject the solution, but the suggestion is that the solution may be "too cold" at the LGM and, more generally, that the derived solution may have persistent regional

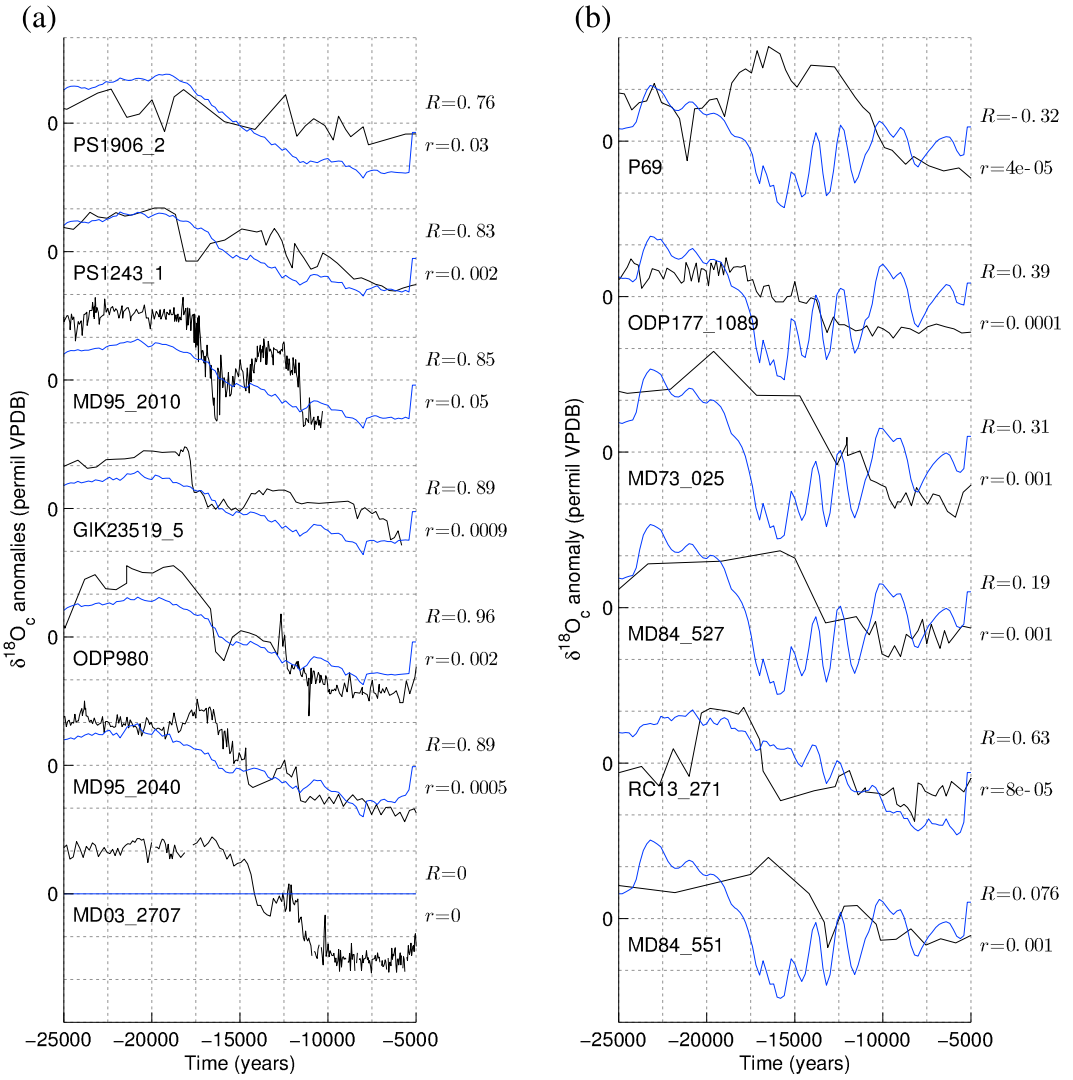

Figure 6. Comparison of 13 planktonic $\delta^{18}O_c$ anomaly records (black curves) and $\delta^{18}O_c$ anomaly records derived from benthic records (blue curves) in the ML regions overlying planktonic core sites in the (a) North Atlantic and (b) Southern Oceans. Panels are ordered by latitude. Pointwise resolvabilities, r (section 3), and Pearson correlations, R, are shown to the right of each panel. Very small values of r (order 10^{-5}) are practically indistinguishable from 0. The vertical grid spacing is 1‰. ML $\delta^{18}O_c$ in the region overlying MD03_2707 lies entirely in the null space of the inverse problem ($r = 0$) and as such is inferred to be 0‰ at all times.

biases from true values. Treating temperature and $\delta^{18}O_w$ as separate tracers and assigning an a priori 0 probability to water temperatures below the freezing point could reduce the apparent bias; this direction is not explored further.

4.2. Comparison of ML $\delta^{18}O_c$ Estimates From Benthic and Planktonic Data

The motivation for deriving $\underline{\tilde{\mathbf{q}}}$ was to compare it to ML conditions, $\underline{\tilde{\mathbf{q}}}^p$, estimated from planktonic foraminiferal $\delta^{18}O_c$ records; misfits (beyond uncertainty) between the two estimates would indicate deviations from the modern circulation. Most planktonic records considered were recovered from high latitudes, where pointwise resolvabilities are highest. Correlations between planktonic $\delta^{18}O_c$ records and time series from $\underline{\tilde{\mathbf{q}}}$ in grid boxes nearest those records range between 0 and 0.96 in the North Atlantic and between −0.32 and 0.63 in the Southern Ocean (Figure 6). Prolonged offsets between the two reconstructions are evident at most locations, and most features on millennial and shorter time scales in planktonic records are not visible in the benthic reconstruction. However, low pointwise resolvabilities indicate that these disagreements are highly uncertain and do not suffice to disprove the null hypothesis of indistinguishable LGM and modern ocean circulations.

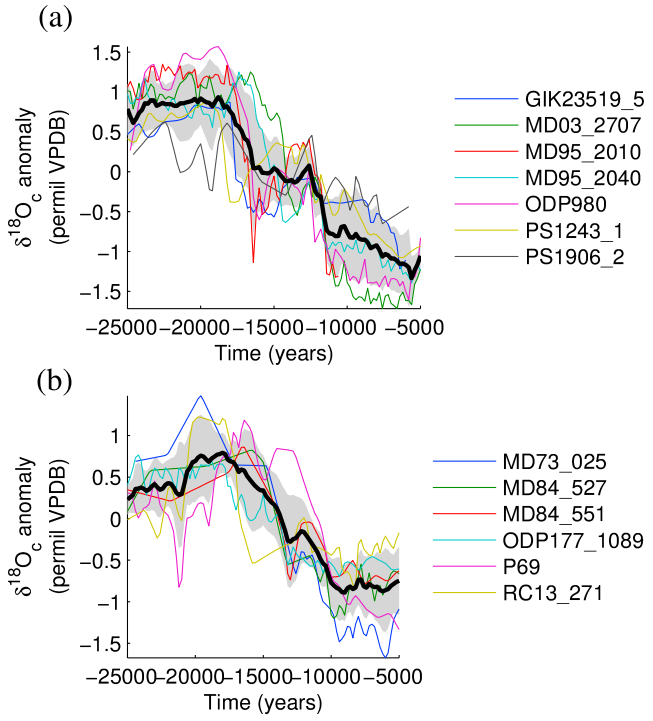

Figure 7. (a) North Atlantic and (b) Southern Ocean planktonic $\delta^{18}O_c$ anomalies overlaid with means removed. Thick black lines are the regional time means computed after smoothing and subsampling each record (see text). Grey bars give the standard deviations of the records about the mean at each time.

Regional averages $\tilde{m}_{NA}(t)$ and $\tilde{m}_{SO}(t)$ of $\underline{\tilde{\mathbf{q}}}$ are more robust and may have more power to test the null hypothesis and identify differences between the deglacial and modern circulations. For comparison, North Atlantic and Southern Ocean averages of planktonic records ($\tilde{m}^p_{NA}(t)$ and $\tilde{m}^p_{SO}(t)$, respectively) are computed (Figure 7). Prior to computing averages, planktonic $\delta^{18}O_c$ records were linearly interpolated to annual resolution, smoothed with a 200 year running mean, and subsampled at 200 year intervals to avoid overweighting averages by more densely sampled records. One sigma uncertainties are approximated by standard deviations of planktonic records computed at every time step; given the sparsity of the data, these estimates should be regarded as lower limits.

Figure 8 compares $\tilde{m}^p_{NA}(t)$, $\tilde{m}^p_{SO}(t)$, $\tilde{m}_{NA}(t)$, and $\tilde{m}_{SO}(t)$. Ideally, a statistical test would be used to evaluate whether planktonic- and benthic-derived estimates agree within error. At present, with few planktonic records, a poor understanding of how and where they represent ML $\delta^{18}O_c$ (described by $\underline{\mathbf{R}}$, see section 3.3) and lacking a robust quantification of their uncertainty, we conclude that regional averages do not differ significantly. Thus, the null hypothesis that the deglacial circulation did not differ from the modern circulation cannot be rejected even when comparing upstream and downstream records on large spatial scales.

5. Discussion

It is worth considering whether the null hypothesis that the past circulation was indistinguishable from the modern is in any danger of being rejected in a statistically rigorous way by the available data. Several studies [*LeGrand and Wunsch*, 1995; *Gebbie and Huybers*, 2006; *Marchal and Curry*, 2008; *Burke et al.*, 2011; *Dail and Wunsch*, 2014] have found that modern ocean circulation estimates adequately represent many observations from the LGM, though *Gebbie* [2014] suggested that $\delta^{13}C$ measurements might individuate the LGM circulation given additional constraints on surface distributions of that tracer. The LGM is arguably better constrained than the deglaciation because data are assumed to represent a steady state.

Rejecting the hypothesis of indistinguishable deglacial and modern circulations using only tracer signals is very difficult because of the space-time filtering along modern tracer transport pathways. Other candidate circulations (such as an ocean with a $\delta^{18}O_c$ residence time of 10^6 years) could likely be readily rejected by the paleo data but would be less relevant to the central question of how past ocean states might have

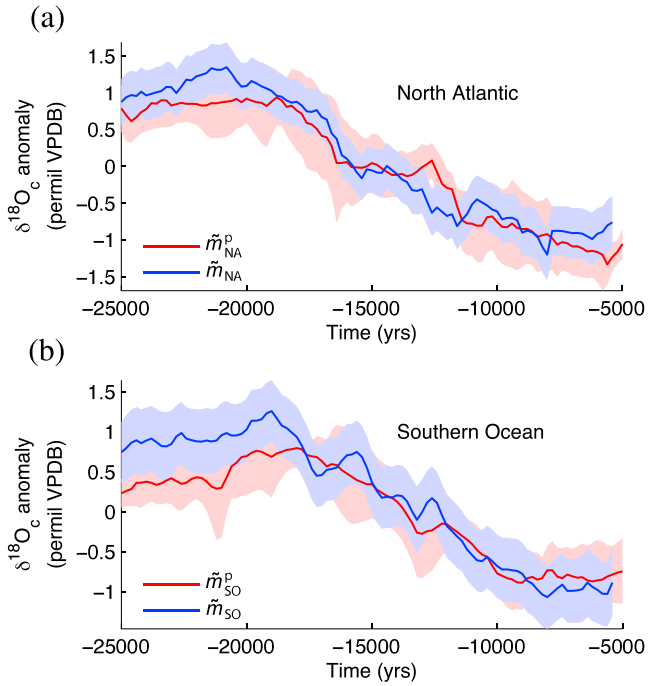

Figure 8. Comparison of spatially averaged ML $\delta^{18}O_c$ anomalies inferred from benthic records in the North Atlantic ($\tilde{m}_{NA}$) and Southern ($\tilde{m}_{SO}$) Oceans to corresponding averages of planktonic $\delta^{18}O_c$ anomalies $\tilde{m}^p_{NA}$ and $\tilde{m}^p_{SO}$. Uncertainties are the same as those described for Figures 5 and 7.

differed from the present. The challenge lies in generating a network of paleoceanographic observations with the power to test the null hypothesis and in representing those observations, along with salient a priori information, in an inverse model. The present framework for using upstream planktonic and downstream benthic records suggests ways forward on both fronts.

To test circulation hypotheses in the upstream-downstream framework, networks of benthic and planktonic records ideally should each be able to constrain all degrees of freedom (that is, all possible spatiotemporal structures) in ML $\delta^{18}O_c$. Short of that ideal, benthic and planktonic networks must be able to constrain a common subset of the spatiotemporal structures. In theory, two records (one benthic and one planktonic) could suffice to distinguish the deglacial circulation from the modern, provided their ML $\delta^{18}O_c$ estimates had sufficiently low uncertainty; in practice, using multiple records of each type is more robust. Consideration of the null space of the benthic inverse problem suggests that low-frequency variability at high latitudes is the best target for reconstruction. Thus, additional high-resolution planktonic data representing high-latitude regions would be valuable, with the goal of estimating the ML $\delta^{18}O_c$ histories of waters that ultimately bathe benthic core sites. Similarly, benthic observations constraining ML $\delta^{18}O_c$ in regions where planktonic records are available would be useful. Benthic records recovered near deepwater formation regions are expected to have better preservation of high-frequency ML signals.

The data importance (defined in section 3.2) indicates the relative roles of benthic sediment core records for constraining the present ML $\delta^{18}O_c$ solution. A value near 1 (the maximum) indicates that the solution is constrained to fit the corresponding record well, whereas values near 0 (the minimum) indicate that the data minimally influence the solution and may be poorly reconstructed as a consequence. Data importance values for the eight benthic sediment core records averaged in time from 20 to 10 ka (the shortened time interval avoids edge effects) range from 0.12 (EI2100) to 0.94 (SA3770) (Table 3). Cores in the North and South Atlantic near deepwater formation sites (where high-frequency ML signals have been attenuated less by ocean transport) have generally higher importance than records from the Indian or Pacific Oceans. The proximity of SA3770 to the Southern Ocean, which is important for setting the $\delta^{18}O_c$ in the global ocean and is poorly constrained by other records, presumably contributes to its particularly high importance.

Table 3. Data Importance for Benthic Records Averaged Over 20–10 ka Calculated From the Data Resolution Matrix $\mathbf{T}_u$

SA1967	NA3223	NA1299	SA3770	EI2100	NA3146	NI1580	EP3210
0.16	0.30	0.29	0.94	0.12	0.25	0.17	0.13

Data importance can be computed for any hypothetical core location (given assumptions about the observational noise) and could be useful for choosing future core recovery sites. The broader question of sediment core location as it applies to experimental design in paleoceanography is a complex subject that should be addressed in a future study. Restrictions due to calcium carbonate preservation, sedimentation rates, bioturbation, and age model construction dramatically limit the set of available core sites.

Prior knowledge of how ocean ML $\delta^{18}O_c$ varies in space and time (i.e., of $\left\langle \underline{\mathbf{qq}}^{\mathrm{T}} \right\rangle$) would reduce the number of unconstrained degrees of freedom in the evolution of ML $\delta^{18}O_c$, thereby making the problem of constraining its evolution more feasible. Such knowledge could be used, for example, by imposing smoothness constraints on the solution, as was done by *Gebbie* [2012] using modern distributions of temperature and $\delta^{18}O_w$. In that study, solution values at high latitudes likely reflected constraints from observations, whereas values elsewhere reflected a priori constraints. Estimating $\left\langle \underline{\mathbf{qq}}^{\mathrm{T}} \right\rangle$ over the last deglaciation is challenging, as it is influenced by complex processes including surface ocean transport, patterns of evaporation and precipitation [*Eisenman et al.*, 2009], and the spreading of low-$\delta^{18}O_c$ waters from melting ice sheets [*Condron and Winsor*, 2011, 2012].

We have ignored uncertainties in record chronologies and assumed a best-case scenario in which published chronologies are correct. Inferences of past circulations from passive tracers are likely sensitive to chronological errors, which artificially phase shift signals. Because the null-space uncertainties are so large, it is unlikely that the fundamental results of this study would be changed by different core chronologies. Explicit descriptions of chronological uncertainties are critical for including that information in inverse modeling studies.

6. Conclusions

The inference of ML $\delta^{18}O_c$ conditions is an important goal in paleoceanography, as surface $\delta^{18}O_c$ changes are related to the Earth's climate. This work was performed with a further goal in mind—the eventual inference of past ocean circulation changes from passive tracers estimated upstream at the ocean surface and downstream in the abyss. Here the modern ocean circulation was found to adequately represent planktonic and benthic $\delta^{18}O_c$ records during the last deglaciation given the large uncertainties estimated for both types of record. This result does not disprove scenarios suggested by *Waelbroeck et al.* [2006, 2011] or *Skinner and Shackleton* [2005] but states that deviations from the modern circulation could not be diagnosed on the basis of the $\delta^{18}O_c$ records considered under the assumptions used in this paper.

An improved understanding of how planktonic observations record ML $\delta^{18}O_c$ (especially at deepwater formation sites, which are best constrained by benthic records) and how ML $\delta^{18}O_c$ covaries in space and time is necessary if benthic and planktonic records are to be used in tandem with tracer transport models to constrain the circulation. Additional highly resolved benthic $\delta^{18}O_c$ records with reliable age models, especially those near deepwater formation sites or in the Southern Ocean, will further constrain the solution toward the goal of differentiating the past circulation from the modern. The analyses presented are also well suited to other geochemical tracers.

Appendix A: Statement of the Inverse Problem

Applying equation (1) recursively, the tracer state vector at time $\mathbf{c}(t_0 + s\Delta t)$ for any time step number $s = 1, 2, \ldots S$ is a linear function of the initial conditions and of the time history of $\mathbf{q}$,

$$\mathbf{c}(t_0 + s\Delta t) = \mathbf{A}^s\mathbf{c}(t_0) + \sum_{k=1}^{s} \mathbf{A}^{k-1}\mathbf{F}\mathbf{q}(t_0 + (s-k)\Delta t). \tag{A1}$$

Substituting equation (A2) into equation (2) yields an expression relating the initial conditions, noise, and ML conditions to the observation $\mathbf{y}(t_0 + s\Delta t)$,

$$\mathbf{y}(t_0 + s\Delta t) = \mathbf{B}\mathbf{A}^s\mathbf{c}(t_0) + \mathbf{B}\sum_{k=1}^{s} \mathbf{A}^{k-1}\mathbf{F}\mathbf{q}\left(t_0 + (s-k)\,\Delta t\right) + \mathbf{n}(t_0 + s\Delta t). \tag{A2}$$

Using $\underline{\mathbf{q}}$ (equation (5)), equation (A3) can be written as

$$\mathbf{y}(t_0 + s\Delta t) = \mathbf{BA}^s\mathbf{c}(t_0) + \mathbf{BG}(s)\underline{\mathbf{q}} + \mathbf{n}(t_0 + s\Delta t), \tag{A3}$$

where $\mathbf{G}(s)$ is the matrix (composed of model Green's functions) whose operation on $\underline{\mathbf{q}}$ gives the summation in equation (A3). Together, the equations for $\mathbf{y}(t_0 + s\Delta t)$ at all times, $t_0, t_0 + \Delta t, \ldots t_0 + S\Delta t$, constitute a simultaneous set of linear equations in terms of $\mathbf{c}(t_0)$, $\underline{\mathbf{q}}$, and $\mathbf{n}$,

$$\begin{bmatrix} \mathbf{y}(t_0) \\ \mathbf{y}\left(t_0 + \Delta t\right) \\ \vdots \\ \mathbf{y}\left(t_0 + S\Delta t\right) \end{bmatrix} = \begin{bmatrix} \mathbf{BA}^0 \\ \mathbf{BA}^1 \\ \vdots \\ \mathbf{BA}^S \end{bmatrix} \mathbf{c}(t_0) + \begin{bmatrix} \mathbf{0} \\ \mathbf{BG}(1) \\ \vdots \\ \mathbf{BG}(S) \end{bmatrix} \underline{\mathbf{q}} + \begin{bmatrix} \mathbf{n}(t_0) \\ \mathbf{n}\left(t_0 + \Delta t\right) \\ \vdots \\ \mathbf{n}\left(t_0 + S\Delta t\right) \end{bmatrix}. \tag{A4}$$

Defining the matrices

$$\underline{\mathbf{A}} = \begin{bmatrix} \mathbf{BA}^0 \\ \mathbf{BA}^1 \\ \vdots \\ \mathbf{BA}^S \end{bmatrix}, \quad \underline{\mathbf{G}} = \begin{bmatrix} \mathbf{0} \\ \mathbf{BG}(1) \\ \vdots \\ \mathbf{BG}(S) \end{bmatrix} \tag{A5}$$

and substituting $\underline{\mathbf{y}}$ and $\underline{\mathbf{n}}$ from equation (5), equation (A5) becomes, collectively for all space and time,

$$\underline{\mathbf{y}} = \underline{\mathbf{A}}\mathbf{c}(t_0) + \underline{\mathbf{G}}\underline{\mathbf{q}} + \underline{\mathbf{n}}. \tag{A6}$$

Defining $\underline{\mathbf{y}}_0 = \underline{\mathbf{A}}\mathbf{c}(t_0)$ yields equation (6).

Appendix B: Computation of Regional Averages and Uncertainties

Regional averages $\tilde{m}_{\mathrm{NA}}(t)$ and $\tilde{m}_{\mathrm{SO}}(t)$ are computed via least squares [*Wunsch*, 2006] as area- and uncertainty-weighted means of $\underline{\tilde{\mathbf{q}}}$ assuming that the deviations of $\underline{\tilde{\mathbf{q}}}$ about true regional means are described by $\mathbf{P}_c$; effects of this assumption are not assessed. Regional means are linear combinations of the elements in $\underline{\tilde{\mathbf{q}}}$, so it is possible to write (for the North Atlantic region; the same procedure is also used in the Southern Ocean) $\tilde{\mathbf{m}}_{\mathrm{NA}} = \mathbf{M}'_{\mathrm{NA}}\underline{\tilde{\mathbf{q}}}$, where $\mathbf{M}'_{\mathrm{NA}}$ is the matrix specifying the mean estimation procedure and $\tilde{\mathbf{m}}_{\mathrm{NA}}$ is $\tilde{m}_{\mathrm{NA}}(t)$ vectorized in time, $\tilde{\mathbf{m}}_{\mathrm{NA}} = \left[\tilde{m}_{\mathrm{NA}}(0), \tilde{m}_{\mathrm{NA}}(\Delta t), \ldots \tilde{m}_{\mathrm{NA}}(S\Delta t)\right]^{\top}$. Similarly, define the matrix $\mathbf{M}_{\mathrm{NA}}$ relating the true area-weighted regional average vector to the true ML conditions, $\mathbf{m}_{\mathrm{NA}} = \mathbf{M}_{\mathrm{NA}}\underline{\mathbf{q}}$. Using the definition of $\mathbf{T}_v$ (equation (11)) and neglecting observational error, the null-space uncertainty due to approximating $\mathbf{m}_{\mathrm{NA}}$ by $\tilde{\mathbf{m}}_{\mathrm{NA}}$ is

$$\left\langle \left(\mathbf{m}_{\mathrm{NA}} - \tilde{\mathbf{m}}_{\mathrm{NA}}\right)\left(\mathbf{m}_{\mathrm{NA}} - \tilde{\mathbf{m}}_{\mathrm{NA}}\right)^{\top} \right\rangle = \left\langle \left(\mathbf{M}_{\mathrm{NA}}\underline{\mathbf{q}} - \mathbf{M}'_{\mathrm{NA}}\underline{\tilde{\mathbf{q}}}\right)\left(\mathbf{M}_{\mathrm{NA}}\underline{\mathbf{q}} - \mathbf{M}'_{\mathrm{NA}}\underline{\tilde{\mathbf{q}}}\right)^{\top} \right\rangle \tag{B1}$$

$$= \left\langle \left(\mathbf{M}_{\mathrm{NA}}\underline{\mathbf{q}} - \mathbf{M}'_{\mathrm{NA}}\mathbf{T}_v\underline{\mathbf{q}}\right)\left(\mathbf{M}_{\mathrm{NA}}\underline{\mathbf{q}} - \mathbf{M}'_{\mathrm{NA}}\mathbf{T}_v\underline{\mathbf{q}}\right)^{\top} \right\rangle \tag{B2}$$

$$= \left(\mathbf{M}_{\mathrm{NA}} - \mathbf{M}'_{\mathrm{NA}}\mathbf{T}_v\right)\left\langle \underline{\mathbf{q}}\underline{\mathbf{q}}^{\top} \right\rangle \left(\mathbf{M}_{\mathrm{NA}} - \mathbf{M}'_{\mathrm{NA}}\mathbf{T}_v\right)^{\top}, \tag{B3}$$

where $\left\langle \underline{\mathbf{q}}\underline{\mathbf{q}}^{\top} \right\rangle$ is the true covariance of $\underline{\mathbf{q}}$. Two choices of $\left\langle \underline{\mathbf{q}}\underline{\mathbf{q}}^{\top} \right\rangle$, chosen as examples, are described in the main text and used to estimate the null-space uncertainty.

Appendix C: Inference of ML $\delta^{18}O_c$ Conditions in a Four-Box Model

This appendix demonstrates a relationship between pointwise resolvability and ventilation rates in a four-box model (Figure C1) using a single benthic $\delta^{18}O_c$ record, NA3146. The utility of column normalizing is also discussed.

Model volumes and fluxes correspond in an order-of-magnitude sense to the geometry and vertical transports of the modern North Atlantic [*Ganachaud and Wunsch*, 2000]. Fluid with $\delta^{18}O_c$ equal to $q_M(t)$ and $q_H(t)$ is transported at constant rates $F_M = 1$ Sv (1 Sv = 10^6 m^3 s^{-1}) and $F_H = 9$ Sv from middle- and high-latitude

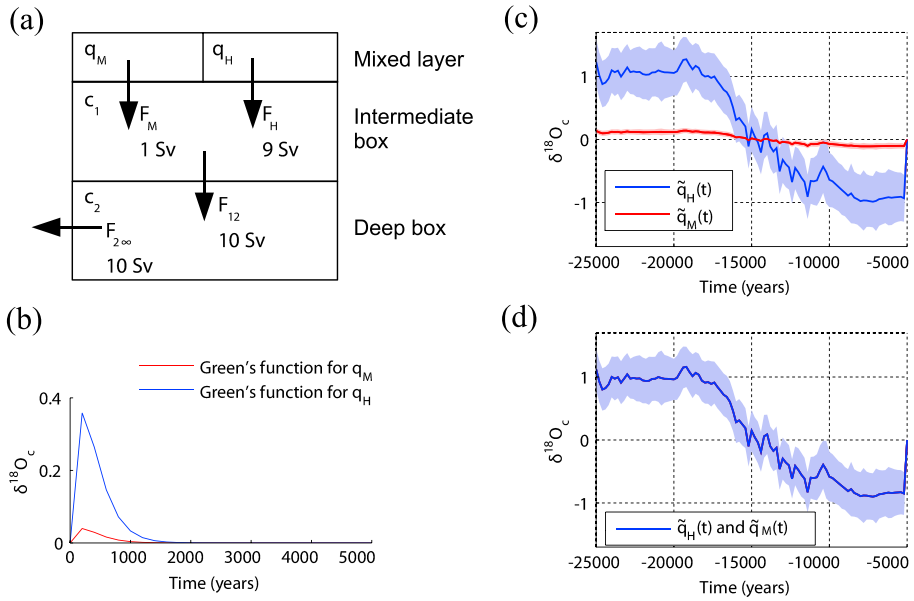

Figure C1. (a) Four-box tracer transport model schematic. The $\delta^{18}O_c$ values q_M and q_H in two ML boxes are injected into box 1 at rates $F_M = 1$ Sv and $F_H = 9$ Sv. Fluid is homogenized in box 1 and flows into box 2 at a rate $F_M + F_H = 10$ Sv, where it subsequently leaves the system. (b) Green's function for q_M (q_H) is generated by stepping equation (C1) forward in time forced by ML conditions that are 0 in both boxes at all times except $q_M(0) = 1$ ($q_H(0) = 1$). ML $\delta^{18}O_c$ anomaly estimates and their standard error are shown in cases (c) without and (d) with column normalization. In both cases, values at 5 ka lie in the null space and are 0, as they are not constrained by benthic observations. In Figure C1d, $\tilde{q}_M(t)$ and $\tilde{q}_H(t)$ are identical. All $\delta^{18}O_c$ values have units of permil VPDB.

ML boxes, respectively, to an intermediate box with volume $V_1 = 10^8$ km^3 and $\delta^{18}O_c$ equal to $c_1(t)$. The intermediate box in turn exchanges fluid at constant rate $F_{12} = 10$ Sv with a deep box with volume $V_2 = 10^8$ km^3 and tracer concentration $c_2(t)$. A compensating flux, $F_{2\infty} = 10$ Sv, evacuates fluid from the deep box out of the system.

The state vector in the four-box model is $\mathbf{c}(t) = \left[c_1(t), c_2(t)\right]^\top$, and the ML vector is $\mathbf{q}(t) = \left[q_M(t), q_H(t)\right]^\top$. Combining the equations for conservation of volume and $\delta^{18}O_c$, the evolution in each box is described by a vector equation in the form of equation (1),

$$\mathbf{c}(t+\Delta t) = \begin{bmatrix} 1-\frac{\Delta t}{\tau_1} & 0 \\ \frac{F_{12}\Delta t}{V_2} & 1-\frac{\Delta t}{\tau_2} \end{bmatrix} \mathbf{c}(t) + \begin{bmatrix} \frac{F_H \Delta t}{V_1} & \frac{F_M \Delta t}{V_1} \\ 0 & 0 \end{bmatrix} \mathbf{q}(t), \tag{C1}$$

where the flushing times, τ_1 and τ_2, are defined as $\tau_1 = V_1/\left(F_M + F_H\right)$ and $\tau_2 = V_2/\left(F_M + F_H\right)$; here $\tau_1 = \tau_2 = 317$ years. Green's functions describing $\delta^{18}O_c$ propagation from the two ML regions to the deep box (Figure C1) are qualitatively similar to those derived from GH12 for the North Atlantic core site (Figure 3). Green's function for q_H is $\frac{F_H}{F_M} = 9$ times larger than that for q_M at all times, a consequence of differing volume fluxes out of the two ML regions. Deep box $\delta^{18}O_c$ is influenced by a sum of ML signals, $q_M(t)$ and $q_H(t)$, lagged and smoothed in time and spatially weighted, similar to the model of GH12.

As in section 4, set $t_0 = -25{,}000$ years, $\Delta t = 200$ years, and the number of times equal to 101. Choose $\mathbf{B} = [0, 1]$ in equation (2) to represent NA3146 as a noisy estimate of deep box $\delta^{18}O_c$. The four-box inverse problem is described by equation (7), where $\underline{\mathbf{G}}$ is constructed (Appendix A) from $\mathbf{B}$ and the matrices in equation (C1), the 101×1 vector $\underline{\mathbf{y}}$ is the objectively mapped NA3146 record, $\underline{\mathbf{n}}$ is a 101×1 vector of observational error, and $\underline{\mathbf{q}}$ is a 202×1 vector of q_M and q_H at all times. Effects of initial conditions are ignored. The problem is row weighted to reflect the objectively mapped uncertainties of NA3146 (section 2).

The problem is solved with and without scaling the columns of $\underline{\mathbf{G}}$ by their norms [*Wunsch*, 2006]. Both the scaled and unscaled problems have $K = 100$ nonzero singular values with the corresponding singular vectors describing variations in q_M and q_H in a fixed ratio at all times except $t = 5000$ years, which is not constrained by the benthic data (due to the finite lag in tracer transport). Information about differences between q_M and q_H is

destroyed en route to box 2 by mixing in box 1; as a result, these differences, at all times, lie in the null space. $K' = K = 100$ is used in both solutions because all nonzero singular values are greater than the observational uncertainties.

The scaled and unscaled solutions are shown in Figure C1. In both cases, the solution exactly reconstructs NA3146 (not shown) except for an initial deviation due to erroneous initial conditions. The unscaled solution is biased so that the solution in each ML location is proportional to the respective volume fluxes into box 1, i.e., $\tilde{q}_H(t)/\tilde{q}_M(t) = F_H/F_M$. By contrast, the scaled solution infers the same values in the two ML regions at all times, so that $\tilde{q}_H(t) = \tilde{q}_M(t)$. Neither solution is truly desirable, but because signals from the two surface boxes are mixed en route to the observations, the data cannot "unmix" spatial gradients and the solutions, $\tilde{q}_H(t)$ and $\tilde{q}_M(t)$, can only be inferred in a fixed ratio. Without scaling the problem, that ratio is set by F_H/F_M, and large spatial gradients, which may be a priori undesirable for ocean tracer distributions, in ML $\delta^{18}O_c$ can be inferred because of the distribution of surface ocean ventilation rates.

The four-box model recovers two characteristic features of the problem solved in section 4. First, scaling by column norms removes spatial gradients but forces ML boxes to covary; this effect is probably responsible for the highly uncertain patterns of spatial covariance inferred in section 4. Second, in the scaled case, pointwise resolvabilities in the two ML boxes are proportional to volume fluxes out of those boxes (and, by extension, to corresponding Green's function amplitudes), $r_M = F_M/(F_H + F_M) = 0.1$ and $r_H = F_H/(F_H + F_M) = 0.9$. This result echoes findings in section 4, though the relationship between r and ventilation rates is expected to be more complex in the many-box model of GH12.

Acknowledgments
Most oxygen isotope records can be obtained through the PANGAEA (pangaea.de/) and NOAA NCDC (www.ncdc.noaa.gov/data-access/paleoclimatology-data/) online archives; the remainder were communicated personally by Delia Oppo, Jerry McManus, Claire Waelbroeck, Luke Skinner, and Simon Jung. For access to MATLAB codes used in analyses and figure making, objectively mapped data, and record ODP980, please contact the corresponding author. The authors acknowledge Ed Boyle, Lloyd Keigwin, Elisabeth Michel, Delia Oppo, David Thornalley, and Claire Waelbroeck for helpful discussions about sediment core records and their interpretation. Thoughtful comments from François Primeau and an anonymous reviewer greatly improved the manuscript.

References

Adkins, J. F., K. McIntyre, and D. P. Schrag (2002), The salinity, temperature, and $\delta^{18}O$ of the glacial deep ocean, *Science*, *298*(5599), 1769–1773.

Amrhein, D. E. (2014), An inverse approach to understanding deglacial benthic oxygen isotope records, Master's thesis, Mass. Inst. of Technol. / Woods Hole Oceanogr. Inst., Cambridge.

Bard, E., M. Arnold, P. Maurice, J. Duprat, J. Moyes, and J.-C. Duplessy (1987), Retreat velocity of the North Atlantic polar front during the last deglaciation determined by ^{14}C accelerator mass spectrometry, *Nature*, *328*(6133), 791–794.

Barker, S., P. Diz, M. Vautravers, J. Pike, G. Knorr, I. Hall, and W. Broecker (2009), Interhemispheric Atlantic seesaw response during the last deglaciation, *Nature*, *457*(7233), 1097–1102.

Bauch, H. A., H. Erlenkeuser, R. F. Spielhagen, U. Struck, J. Matthiessen, J. Thiede, and J. Heinemeier (2001), A multiproxy reconstruction of the evolution of deep and surface waters in the subarctic Nordic seas over the last 30,000 yr, *Quat. Sci. Rev.*, *20*(4), 659–678.

Bemis, B., H. Spero, J. Bijma, and D. Lea (1998), Reevaluation of the oxygen isotopic composition of planktonic foraminifera: Experimental results and revised paleotemperature equations, *Paleoceanography*, *13*(2), 150–160.

Bretherton, F. P., R. E. Davis, and C. Fandry (1976), A technique for objective analysis and design of oceanographic experiments applied to MODE-73, in *Deep Sea Research and Oceanographic Abstracts*, vol. 23, pp. 559–582, Elsevier, Oxford, U. K.

Bronk Ramsey, C. (2009), Bayesian analysis of radiocarbon dates, *Radiocarbon*, *51*(1), 337–360.

Bryden, H. L. (1973), New polynomials for thermal expansion, adiabatic temperature gradient and potential temperature of sea water, in *Deep Sea Research and Oceanographic Abstracts*, vol. 20, pp. 401–408, Elsevier, Oxford, U. K.

Burke, A., O. Marchal, L. I. Bradtmiller, J. F. McManus, and R. François (2011), Application of an inverse method to interpret $^{231}Pa/^{230}Th$ observations from marine sediments, *Paleoceanography*, *26*, PA1212, doi:10.1029/2010PA002022.

Charles, C. D., P. N. Froelich, M. A. Zibello, R. A. Mortlock, and J. J. Morley (1991), Biogenic opal in Southern Ocean sediments over the last 450,000 years: Implications for surface water chemistry and circulation, *Paleoceanography*, *6*(6), 697–728.

Condron, A., and P. Winsor (2011), A subtropical fate awaited freshwater discharged from glacial Lake Agassiz, *Geophys. Res. Lett.*, *38*, L03705, doi:10.1029/2010GL046011.

Condron, A., and P. Winsor (2012), Meltwater routing and the Younger Dryas, *Proc. Nat. Acad. Sci.*, *109*(49), 19,928–19,933.

Conkright, M. E., S. Levitus, and T. P. Boyer (1994), *World Ocean Atlas: 1994 Nutrients*, vol. 1, NOAA Atlas NESDIS 1, Washington, D. C.

Curry, W., and D. Oppo (2005), Glacial water mass geometry and the distribution of $\delta^{13}C$ of ΣCO_2 in the western Atlantic Ocean, *Paleoceanography*, *20*, PA1017, doi:10.1029/2004PA001021.

Dail, H., and C. Wunsch (2014), Dynamical reconstruction of upper-ocean conditions in the Last Glacial Maximum Atlantic, *J. Clim.*, *27*(2), 807–823.

Dokken, T. M., and E. Jansen (1999), Rapid changes in the mechanism of ocean convection during the last glacial period, *Nature*, *401*(6752), 458–461.

Eisenman, I., C. Bitz, and E. Tziperman (2009), Rain driven by receding ice sheets as a cause of past climate change, *Paleoceanography*, *24*, PA4209, doi:10.1029/2009PA001778.

Fofonoff, P., and R. Millard (1983), *Algorithms for Computation of Fundamental Properties of Seawater, UNESCO Technical Papers in Marine Science*, UNESCO, Paris.

Ganachaud, A., and C. Wunsch (2000), Improved estimates of global ocean circulation, heat transport and mixing from hydrographic data, *Nature*, *408*(6811), 453–457.

Gebbie, G. (2012), Tracer transport timescales and the observed Atlantic-Pacific lag in the timing of the Last Termination, *Paleoceanography*, *27*, PA3225, doi:10.1029/2011PA002273.

Gebbie, G. (2014), How much did Glacial North Atlantic Water shoal?, *Paleoceanography*, *29*, 190–209, doi:10.1002/2013PA002557.

Gebbie, G., and P. Huybers (2006), Meridional circulation during the Last Glacial Maximum explored through a combination of South Atlantic $\delta^{18}O$ observations and a geostrophic inverse model, *Geochem. Geophys. Geosyst.*, *7*, Q11N07, doi:10.1029/2006GC001383.

Gebbie, G., and P. Huybers (2010), Total matrix intercomparison: A method for resolving the geometry of water-mass pathways, *J. Phys. Oceanogr.*, *40*(8), 1710–1728.

Gebbie, G., and P. Huybers (2011), How is the ocean filled?, *Geophys. Res. Lett.*, *38*, L06604, doi:10.1029/2011GL046769.
Gebbie, G., and P. Huybers (2012), The mean age of ocean waters inferred from radiocarbon observations: Sensitivity to surface sources and accounting for mixing histories, *J. Phys. Oceanogr.*, *42*(2), 291–305.
Gouretski, V., and K. P. Koltermann (2004), WOCE global hydrographic climatology, *Ber. des BSH*, *35*, 1–52.
Hays, J., J. Imbrie, and N. Shackleton (1976), Variations in the Earth's orbit: Pacemaker of the ice ages, *Science*, *194*, 1121–1134.
Hodell, D. A., C. D. Charles, J. H. Curtis, P. G. Mortyn, U. S. Ninnemann, and K. A. Venz (2003), *Data Report: Oxygen Isotope Stratigraphy of ODP Leg 177 Sites 1088, 1089, 1090, 1093, and 1094*, 1–26, edited by R. Gersonde, D. A. Hodell, and P. Blum, Proc. ODP, Sci. Results, 177, Ocean Drilling Program, College Station, Tex.
Hüls, M., and R. Zahn (2000), Millennial-scale sea surface temperature variability in the western tropical North Atlantic from planktonic foraminiferal census counts, *Paleoceanography*, *15*(6), 659–678.
Ivanochko, T., R. Ganeshram, G. Brummer, G. Ganssen, S. Jung, S. Moreton, and D. Kroon (2005), Variations in tropical convection as an amplifier of global climate change at the millennial scale, *Earth Planet. Sci. Lett.*, *235*(1–2), 302–314.
Jung, S., G. Ganssen, and G. Davies (2001), Multidecadal variations in the early Holocene outflow of Red Sea water into the Arabian Sea, *Paleoceanography*, *16*(6), 658–668.
Jung, S., D. Kroon, G. Ganssen, F. Peeters, and R. Ganeshram (2009), Enhanced Arabian Sea intermediate water flow during glacial North Atlantic cold phases, *Earth Planet. Sci. Lett.*, *280*(1–4), 220–228.
Keigwin, L. D. (2004), Radiocarbon and stable isotope constraints on Last Glacial Maximum and Younger Dryas ventilation in the western North Atlantic, *Paleoceanography*, *19*, PA4012, doi:10.1029/2004PA001029.
Key, R. M., A. Kozyr, C. L. Sabine, K. Lee, R. Wanninkhof, J. L. Bullister, R. A. Feely, F. J. Millero, C. Mordy, and T.-H. Peng (2004), A global ocean carbon climatology: Results from Global Data Analysis Project (GLODAP), *Global Biogeochem. Cycles*, *18*, GB4031, doi:10.1029/2004GB002247.
Labracherie, M., L. D. Labeyrie, J. Duprat, E. Bard, M. Arnold, J.-J. Pichon, and J.-C. Duplessy (1989), The last deglaciation in the Southern Ocean, *Paleoceanography*, *4*(6), 629–638.
LeGrand, P., and C. Wunsch (1995), Constraints from paleotracer data on the North Atlantic circulation during the last glacial maximum, *Paleoceanography*, *10*(6), 1011–1045.
LeGrande, A., and G. Schmidt (2006), Global gridded data set of the oxygen isotopic composition in seawater, *Geophys. Res. Lett.*, *33*, L12604, doi:10.1029/2006GL026011.
Little, M., R. Schneider, D. Kroon, T. Price, T. Bickert, and G. Weger (1997), Rapid palaeoceanographic changes in the Benguela Upwelling System for the last 160,000 years as indicated by abundances of planktonic foraminifer, *Palaeogeogr. Palaeoclimatol. Palaeoecol.*, *130*, 135–161.
Liu, Z., et al. (2009), Transient simulation of last deglaciation with a new mechanism for Bølling-Allerød warming, *Science*, *325*(5938), 310–314.
Lund, D., J. Adkins, and R. Ferrari (2011), Abyssal Atlantic circulation during the Last Glacial Maximum: Constraining the ratio between transport and vertical mixing, *Paleoceanography*, *26*, PA1213, doi:10.1029/2010PA001938.
Manabe, S., and R. Stouffer (1988), Two stable equilibria of a coupled ocean-atmosphere model, *J. Clim.*, *1*(9), 841–866.
Marchal, O., and W. B. Curry (2008), On the abyssal circulation in the glacial Atlantic, *J. Phys. Oceanogr.*, *38*(9), 2014–2037.
McDougall, T. J., and P. M. Barker (2011), *Getting Started With TEOS-10 and the Gibbs Seawater (GSW) Oceanographic Toolbox*, 28 pp., SCOR/IAPSO WG 127, Sydney.
McManus, J., R. Francois, J. Gherardi, L. Keigwin, and S. Brown-Leger (2004), Collapse and rapid resumption of Atlantic meridional circulation linked to deglacial climate changes, *Nature*, *428*(6985), 834–837.
Millo, C., M. Sarnthein, A. Voelker, and H. Erlenkeuser (2006), Variability of the Denmark Strait overflow during the last glacial maximum, *Boreas*, *35*(1), 50–60.
Nees, S., and J. Thiede (1993), (Appendix 3) Stable isotope record of Neogloboquadrina pachyderma of sediment core PS1906-2 in the Greenland Sea, doi:10.1594/PANGAEA.66896, In Supplement to: Nees, Stefan (1993): Spätquartäre Benthosforaminiferen des Europäischen Nordmeeres: Veränderungen der Artengesellschaften und Akkumulationsraten bei Klimawechseln. Berichte aus dem Sonderforschungsbereich 313, Christian-Albrechts-Universität, Kiel, 44, 80 pp, doi:10.2312/reports-sfb313.1993.44.
Nelson, C., I. Hendy, H. Neil, C. Hendy, and P. Weaver (2000), Last glacial jetting of cold waters through the Subtropical Convergence zone in the Southwest Pacific off eastern New Zealand, and some geological implications, *Palaeogeogr. Palaeoclimatol. Palaeoecol.*, *156*(1), 103–121.
Ostermann, D., and W. Curry (2000), Calibration of stable isotopic data: An enriched $\delta^{18}O$ standard used for source gas mixing detection and correction, *Paleoceanography*, *15*(3), 353–360.
Otto-Bliesner, B., C. Hewitt, T. Marchitto, E. Brady, A. Abe-Ouchi, M. Crucifix, S. Murakami, and S. Weber (2007), Last Glacial Maximum ocean thermohaline circulation: PMIP2 model intercomparisons and data constraints, *Geophys. Res. Lett.*, *34*, L12706, doi:10.1029/2007GL029475.
Peacock, S., and M. Maltrud (2006), Transit-time distributions in a global ocean model, *J. Phys. Oceanogr.*, *36*(3), 474–495.
Pichon, J.-J., L. D. Labeyrie, G. Bareille, M. Labracherie, J. Duprat, and J. Jouzel (1992), Surface water temperature changes in the high latitudes of the Southern Hemisphere over the Last Glacial-Interglacial Cycle, *Paleoceanography*, *7*(3), 289–318.
Preisendorfer, R. W., and C. D. Mobley (1988), *Principal Component Analysis in Meteorology and Oceanography*, vol. 425, Elsevier, New York.
Press, W. H., G. B. Rybicki, and J. N. Hewitt (1992), The time delay of gravitational lens 0957+ 561. I—Methodology and analysis of optical photometric data. II—Analysis of radio data and combined optical-radio analysis, *Astrophys. J.*, *385*, 404–420.
Reimer, P., et al. (2009), INTCAL09 and MARINE09 radiocarbon age calibration curves, 0–50,000 years calendar BP, *Radiocarbon*, *51*(4), 1111–1150.
Rubin, S. I., and R. M. Key (2002), Separating natural and bomb-produced radiocarbon in the ocean: The potential alkalinity method, *Global Biogeochem. Cycles*, *16*(4), 1105, doi:10.1029/2001GB001432.
Rühlemann, C., S. Mulitza, P. Muller, G. Wefer, and R. Zahn (1999), Warming of the tropical Atlantic Ocean and slowdown of thermohaline circulation during the last deglaciation, *Nature*, *402*(6761), 511–514.
Rutberg, R., and S. Peacock (2006), High-latitude forcing of interior ocean $\delta^{13}C$, *Paleoceanography*, *21*, PA2012, doi:10.1029/2005PA001226.
Rybicki, G. B., and W. H. Press (1992), Interpolation, realization, and reconstruction of noisy, irregularly sampled data, *Astrophys. J.*, *398*, 169–176.
Saunders, P. M. (1981), Practical conversion of pressure to depth, *J. Phys. Oceanogr.*, *11*, 573–578.
Schönfeld, J., R. Zahn, and L. de Abreu (2003), Surface and deep water response to rapid climate changes at the Western Iberian Margin, *Global Planet. Change*, *36*(4), 237–264.

Shackleton, N., J.-C. Duplessy, M. Arnold, P. Maurice, M. Hall, and J. Cartlidge (1988), Radiocarbon age of last glacial Pacific deep water, *Nature*, *335*(6192), 708–711.

Shackleton, N., R. Fairbanks, T.-C. Chiu, and F. Parrenin (2004), Absolute calibration of the Greenland time scale: Implications for Antarctic time scales and for $\Delta^{14}C$, *Quat. Sci. Rev.*, *23*(14), 1513–1522.

Skinner, L., and N. Shackleton (2004), Rapid transient changes in northeast Atlantic deep water ventilation age across Termination I, *Paleoceanography*, *19*, PA2005, doi:10.1029/2003PA000983.

Skinner, L., and N. Shackleton (2005), An Atlantic lead over Pacific deep-water change across Termination I: Implications for the application of the marine isotope stage stratigaphy, *Quat. Sci. Rev.*, *24*, 571–580.

Skinner, L., N. Shackleton, and H. Elderfield (2003), Millennial-scale variability of deep-water temperature and $\delta^{18}O_{dw}$ indicating deep-water source variations in the Northeast Atlantic, 0–34 cal. ka BP, *Geochem. Geophys. Geosyst.*, *4*(12), 1098, doi:10.1029/2003GC000585.

Skinner, L., S. Fallon, C. Waelbroeck, E. Michel, and S. Barker (2010), Ventilation of the deep Southern Ocean and deglacial CO_2 rise, *Science*, *328*(5982), 1147–1151.

Vidal, L., R. Schneider, O. Marchal, T. Bickert, T. Stocker, and G. Wefer (1999), Link between the North and South Atlantic during the Heinrich events of the last glacial period, *Clim. Dyn.*, *15*(12), 909–919.

Waelbroeck, C., C. Levi, J. Duplessy, L. Labeyrie, E. Michel, E. Cortijo, F. Bassinot, and F. Guichard (2006), Distant origin of circulation changes in the Indian Ocean during the last deglaciation, *Earth Planet. Sci. Lett.*, *243*(1–2), 244–251.

Waelbroeck, C., L. Skinner, L. Labeyrie, J. Duplessy, E. Michel, N. Riveiros, J. Gherardi, and F. Dewilde (2011), The timing of deglacial circulation changes in the Atlantic, *Paleoceanography*, *26*, PA3213, doi:10.1029/2010PA002007.

Weldeab, S., D. W. Lea, R. R. Schneider, and N. Anderson (2007), 155,000 years of West African monsoon and ocean thermal evolution, *Science*, *316*(5829), 1303–1307.

Winguth, A., D. Archer, E. Maier-Reimer, and U. Mikolajewicz (2000), Paleonutrient data analysis of the glacial Atlantic using an adjoint ocean general circulation model, in *Inverse Methods in Global Biogeochemical Cycles*, edited by P. Kasibhatla et al., AGU, Washington, D. C.

Wunsch, C. (2006), *Discrete Inverse and State Estimation Problems: With Geophysical Fluid Applications*, Cambridge Univ. Press, Cambridge, U. K.

Wunsch, C., and P. Heimbach (2008), How long to oceanic tracer and proxy equilibrium?, *Quat. Sci. Rev.*, *27*(7–8), 637–651.

Zahn, R., and A. Stüber (2002), Suborbital intermediate water variability inferred from paired benthic foraminiferal Cd/Ca and $\delta^{13}C$ in the tropical West Atlantic and linking with North Atlantic climates, *Earth Planet. Sci. Lett.*, *200*(1–2), 191–205.

Zarriess, M., and A. Mackensen (2010), The tropical rainbelt and productivity changes off northwest Africa: A 31,000-year high-resolution record, *Mar. Micropaleontol.*, *76*(3–4), 76–91.

Zarriess, M., and A. Mackensen (2011), Testing the impact of seasonal phytodetritus deposition on $\delta^{13}C$ of epibenthic foraminifer Cibicidoides wuellerstorfi: A 31,000 year high-resolution record from the northwest African continental slope, *Paleoceanography*, *26*, PA2202, doi:10.1029/2010PA001944.